Hybrid star within the framework of a lowest-order constraint variational method

S. Khanmohamadi* and H. R. Moshfegh†
Department of Physics, University of Tehran, P.O. Box 14395-547 Tehran, Iran

S. Atashbar Tehrani‡
School of Particles and Accelerators, Institute for Research in Fundamental Sciences (IPM), P.O. Box 19395-5531 Tehran, Iran

(Received 22 July 2019; revised manuscript received 30 October 2019; published 6 January 2020)

The hadron-quark phase transition in the core of heavy neutron star (NS) has been studied. For the hadronic sector, we have used the lowest-order constraint variational method by employing AV_{18}, AV_{14}, UV_{14}, and Reid 68 two-body nucleon-nucleon forces supplemented by the phenomenological Urbana-type three-body force. We have adopted the MIT bag model as well as three-flavor version of the Nambu–Jona-Lasinio (NJL) model to describe the quark phase. The equation of state (EOS) of a hybrid star (HS) is presented by combining two EOS of the hadronic sector and quark sector of a star, which are derived from independent models or theories. The hadron-quark transition is constructed by considering a sharp phase transition, i.e., Maxwell construction. The structure of the HS is calculated and reported by solving Tolman-Oppenheimer-Volkoff equations. Finally, the radii and tidal deformability of purely NS and HS for the mass of 1.4 $M_\odot$ is computed, and new constraints on these quantities are checked. The maximum mass of the HS is found more than 2 $M_\odot$ for both the NJL and MIT bag models. However, the maximum mass of 1.796 $M_\odot$ (1.896 $M_\odot$) was the best result that would be calculated for a stable HS with the pure quark core within the MIT (NJL) model. All the hybrid EOS fulfill the constraints on radii and tidal deformability extracted from the binary GW170817 for HSs. A comprehensive analysis on the structure of purely NS and HS and also compactness, tidal Love number, and tidal deformability for the star with the mass of 1.4 $M_\odot$ has been conducted for various EOS of the hadron sector and several parameter sets of the quark EOS. The results achieved in this study are in good concurrence with the other calculations reported on this subject.

DOI: 10.1103/PhysRevD.101.023004

I. INTRODUCTION

One of the issues in the context of the compact stars is the probable appearance of the quark degrees of freedom in the interior of the heavy neutron stars (NSs) [1–3]. The question of whether or not quark matter exists in the core of NSs has newly received interest [4–6], by the discovery of two massive neutron stars [7–11]. Microscopic calculations demonstrate that in heavy NSs ($M \approx 2\ M_\odot$) the density of the core reaches to around 1 fm^{-3}, and at such high densities, the Fermi energy level of particles increases enough to produce various exotic particles, and the appearance of the quark phase (in addition to the baryonic phase) is not unexpected [12]. In fact, in densities above nuclear saturation density ($\rho \gg \rho_0 = 0.16$ fm^{-3}), some other exotic particles may exist in the interior of a NS in addition to nucleons and leptons, such as hyperons and π and k condensation. In higher densities, nuclear matter may experience phase transition to a deconfined quark plasma of u, d, and s quarks. However, the appearance of hyperons in beta stable matter would strongly decrease the maximum mass of the star [13–17]; therefore, in this situation, the presentation of a nonbaryonic phase like the quark matter could be a feasible way to stiffen the EOS and reach to a massive NS. Thus, a heavy NS can be a hybrid star [18]. It would have been ideal if there had been a unified theory which could have treated both the hadronic and quark phases simultaneously in all ranges of temperatures and densities, but, unfortunately, there is no such reliable theory as of now. However, at finite temperature and zero baryon density, a numerical study on lattice formalism in QCD has provided some reliable results for physics of the deconfinement transition [19,20]. In this case, lattice calculations predict that the deconfinement happens via a smooth crossover transition [21] at a temperature, $T \approx$180–200 MeV [22,23]. However, studies at finite baryon densities on the lattice are very difficult. Some progress has been made in recent years in extending the calculations to finite quark chemical potential;

*s.khanmohamadi@ut.ac.ir
†hmoshfegh@ut.ac.ir
‡Atashbar@ipm.ir

however, they have not yet provided reliable results [24,25]. Therefore, studying the EOS and phase transition of nuclear matter to the deconfinement quark phase at zero temperature and high densities, which is the case in NSs, from the first principles, is a difficult task due to the nonlinear and nonperturbative nature of the QCD governing on the behavior of such systems.

Therefore, as a starting point, one can use some phenomenological models for describing the quark matter. Over the past few decades, many authors have intensively studied various aspects related to the formation of exotic degrees of freedom in neuron stars and proposed observational tests which confirm the existence of such constituents in the interior of compact stars (see, Ref. [26] and references therein). The structure and properties of hybrid stars (HSs) have been studied in several papers with different hadron and quark models and various types of phase transitions. In Refs. [12,27–33], a few of them are reported.

We employ the MIT bag and Nambu–Jona-Lasinio (NJL) models for describing quark matter in this paper. The MIT bag model builds confinement and asymptotic freedom via a phenomenological model and is essentially an enhanced version of Bogoliubov's model for quarks that are considered three massless quarks in a vacuum cavity of radius R with a finite, spherical, square well potential. Bogoliubov's model has a few shortcomings such as the violation of energy-momentum conservation [34]. The MIT bag model solves this problem by the inclusion of phenomenological confining pressure, which is named the bag constant, B [35]. This prescription provides a mechanism for natural confinement and also causes the model to become a Lorentz-covariant model. To describe the quark phase, an improved version of the MIT bag model, in which interaction between u, d, and s quarks inside the bag are taken in a one gluon-exchange approximation, was used [5,36–38].

Besides, we adopt the three-flavor version of the NJL model to describe the deconfined quark phase. The NJL model contains some of the basic symmetries of QCD, namely, chiral symmetry. The most important feature of the NJL model is its nontrivial vacuum by breaking the chiral symmetry dynamically by spontaneous mass generation. In the NJL model, at the low-energy scale, the gluon acquires a large effective mass that can be integrated out to a good approximation, leaving a local contact four-fermion interaction between the quarks. Upon this procedure, the confinement was lost because the local color symmetry of QCD was reduced to a global symmetry. This drawback of the NJL model is not an issue when modeling quark matter at high densities, since the quark matter is deconfined at high densities. The NJL model has been very successful in describing the vacuum properties of low-lying meosns and predicts at sufficiently high densities or temperatures a phase transition to a chiral symmetric state [39–42]. Strictly speaking, the NJL model is usable in vacuum and at high densities but not in the hadronic phase in between.

Contrary to the quark matter case, microscopic theories of the nucleonic EOS have reached a high degree of sophistication. We employ the lowest-order constraint variational (LOCV) method for describing the nucleonic sector. The LOCV method is a well-known many-body technique that was originally used to study the properties of cold symmetric nuclear matter [43,44] by using the Ried-type potential [45,46] as the bare two-body forces (2BF). Later on, this approach was extended to finite temperature [47], and also calculations of the EOS of asymmetric nuclear matter [48], pure neutron matter, and β-stable matter [49,50] were carried out within this framework by using more sophisticated potentials. Moreover, relativistic corrections have been considered in calculating thermodynamic properties of nuclear matter within this model at both zero and finite temperatures [51,52]. Recently, this technique has been extended by adding three-body force (TBF) to this formalism [53,54] and has been used to study the structure of the NS [53] as well as a protoneutron star [54]. This model is successful in reproducing the correct saturation point parameters such as $E_{\rm sym}(\rho_0, L,$ and $K_{\rm sym})$ by using a revised version of TBF which is based on an isospin-dependent parametrization of coefficient in the Urbana-type (UIX) forces. Within the LOCV formalism employing AV_{18} supplemented by TBF in Urbana type [54] and chiral symmetry [55], the maximum NS mass is obtained above 2 $M_\odot$. Recently, the LOCV method is reformulated to extract the EOS of Hyper nuclear matter [56,57].

For the region of phase transition, a detailed study employing the Wigner-Seitz cell approach [58] suggests that the mixed phase behaves more in accordance with the Maxwell construction than the Gibbs construction. It may happen that a hadron-quark mixed phase is unlikely to be stable for a reasonable value of surface tension [58–60]; then, the situation is closer to the Maxwell construction case, in which two pure phases are in direct contact with each other. Therefore, we restrict ourselves to analyzing the sharp hadron to quark matter phase transition. Maxwell construction and Gibbs construction describe the first-order phase transition. The existence of the "mass twins" in the mass radius relationship for the compact star also seems to support the Maxwell construction viewpoint [61]. Some authors argue that the phase transition could be crossover, which may lead to interpolation/percolation construction [62,63]. As we mentioned above, the lattice QCD calculation shows that the transition line for low baryon densities is a crossover [64–67] but it is model dependent for high densities and low temperatures. Thus, it should completely be treated phenomenologically in this case.

Nowadays, an EOS should not only fulfill the maximum mass constraints, $2.01^{+0.04}_{-0.04} \leq M_{\rm TOV}/M_\odot \lesssim 2.16^{+0.17}_{-0.15}$, but

should additionally fulfill the new constraint on radii and tidal deformability of compact stars set by the binary NS system, GW170817 [68]. The brand new era of multimessenger astronomy started on August 17, 2017, with the first direct detection of both gravitational and electromagnetic radiation from the binary NS merger GW170817, which was recorded by the Advanced LIGO and Virgo network of gravitational wave recorders [69,70]. GW170817 established for the first time the association of short gamma-ray bursts with NS mergers, which can help solve the long-standing puzzle of the origin of these phenomena [71–74]. GW170817 gives fundamental new insights into the nature of dense matter by adding the tidal deformability (polarizability) constraints on EOS. The tidal deformability, Λ, encodes the response of NS to the external tidal field produced by its companion similar to the response of a polar molecular to an external electrical field. We calculate the tidal deformability and radii of the NSs and HSs that exist in this paper with the mass of 1.4 $M_\odot$, and new constraints on these quantities are checked.

The paper is organized as follows. In Sec. II A, we will address the nucleonic matter and briefly review the determination of baryonic EOS in beta equilibrium in the LOCV approach at zero temperature. Section II B is concerned the quark matter EOS according to the MIT and NJL models. In Sec. III A, by using these models, a hybrid equation of state is obtained, assuming a Maxwell construction. In Sec. III B, the structure of the hybrid star is presented. Section III C is concerned with calculating the tidal deformability, and Sec. IV is devoted to the summary of the results and conclusions.

II. EQUATION OF STATE

The neutron star outer and inner crust exist at densities between $10^4 \leq \epsilon_{\rm crust} \leq 10^{14}$ gr cm^{-3} [75]. Matter in the inner crust consists mostly of nuclei in a Coulomb lattice that is immersed in a gas of electrons and, above neutron drip (greater than or equal to $4 * 10^{11}$ gr cm^{-3}), free neutrons. In densities above the saturation density (greater than or equal to 10^{14} gr cm^{-3}), the relevant degrees of freedom are hadrons. At higher densities (several times the saturation density), baryons begin to overlap and lose their individuality, and to describe the medium, the quark degrees of freedom need to be included. In this work, we use the Harrison-Wheeler equation of state for the neutron star crust.

A. Confined hadronic phase

Different theoretical approaches can be used to calculate empirical properties of infinite nuclear matter. In recent years, experimental observations, together with theoretical efforts for explaining and analyzing them, have provided reliable microscopic models for describing nuclear matter. In this research, we use the LOCV model, which is a microscopic model based on cluster expansion and is in a good agreement with empirical properties. In this section, we briefly review the LOCV method, the details of which can be found in the references in the Introduction. First, we restrict our attention to the baryonic matter and the procedure of adding TBF to the LOCV formalism; then, we employ this formalism to extract the EOS of the β stable matter.

1. Asymmetric nuclear matter

For the first step in the LOCV formalism, a trial wave function of the N-body interacting system at zero temperature is produced as

$$\Psi(1\ldots N) = F(1\ldots N)\Phi(1\ldots N), \tag{1}$$

where $\Phi(1\ldots N)$ is a noninteracting ground-state wave function of N independent nucleons and $F(1\ldots N)$ is a N-body correlation operator. The correlation operator is obtained in the Jastrow approximation, which is the symmetrized product of two-body correlation function operators, which is written as

$$F(1\ldots N) = \mathcal{S}\prod_{i>j} f(ij), \tag{2}$$

where $\mathcal{S}$ is the symmetrizing operator. $f(ij)$ is read as

$$f(ij) = \sum_{\alpha,p=1}^{3} f_\alpha^p(ij) O_\alpha^p(ij), \tag{3}$$

where $\alpha = \{J, L, S, T, T_z\}$ [total (J), orbital (L), spin (S) angular momentum, and isospin (T) the and third component of isospin T_z] and $p = 2,\ 3$ is used for coupled channels with $J = L \pm 1$. Otherwise, p is set to unity. The operators $O_\alpha^p(ij)$ are written as

$$O_\alpha^{p=1-3} = 1, \left(\frac{2}{3} + \frac{1}{6}S_{12}\right), \left(\frac{1}{3} - \frac{1}{6}S_{12}\right), \tag{4}$$

where $S_{12} = 3(\sigma_1.\hat{r})(\sigma_2.\hat{r}) - \sigma_1.\sigma_2$ is the usual tensor operator. In general, the nuclear Hamiltonian is read as a sum of the nonrelativistic single-particle kinetic energy and potential

$$H = \sum_i \frac{p_i^2}{2m_i} + \sum_{i<j} V(ij) + \cdots. \tag{5}$$

The baryonic energy expectation value E_B is considered as the sum of one body energy, E_1 and two-body energy, E_2 and written as:

$$E_B[f] = \frac{1}{N}\frac{\langle\Psi|H|\Psi\rangle}{\langle\Psi|\Psi\rangle} = E_1 + E_{MB} \cong E_1 + E_2, \quad (6)$$

in which

$$E_1 = \sum_i \frac{3\hbar^2 (k_i^F)^2}{10 m_i}, \quad (7)$$

where $i = n,\ p$, and k_i^F is the corresponding nucleon momentum divided by $\hbar$ and E_2 is defined as

$$E_2 = \frac{1}{2N}\sum_{ij}\langle ij|W(12)|ij - ji\rangle, \quad (8)$$

with

$$W(12) = -\frac{\hbar^2}{2m}[f(12), [\nabla_{12}^2, f(12)]] + f(12)V(12)f_T(12). \quad (9)$$

Higher-order terms in the cluster expansion series are neglectable [47]. This expression is now minimized with respect to the channel correlation functions but subjected to the normalization constraint, which is considered as [47,76,77]

$$\frac{1}{N}\sum_{ij}\langle ij|h_{T_z}^2(12) - f^2(12)|ij - ji\rangle = 0. \quad (10)$$

The condition of healing the correlation functions to the Pauli function $h_{T_z}(12)$, which for the asymmetric matter takes the following form, is also imposed [77],

$$h_{T_z}(r) = \left[1 - \frac{9}{2}\left(\frac{J_1(k_i^F r)}{k_i^F r}\right)^2\right]^{-\frac{1}{2}}, \quad T_z = \pm 1$$
$$= 1, \quad T_z = 0, \quad (11)$$

with $J_1(x)$ being the spherical Bessel function of order 1. The normalization constraint introduces the Lagrangian multiplier parameters in the LOCV formalism. The procedure of minimizing Eq. (9) provides a number of Euler-Lagrange differential equations for functions $f_\alpha^p(ij)$. Solving these equations leads to the determination of correlation functions and then the two-body cluster energy. In the nuclear matter calculations, the saturation properties of cold symmetric nuclear matter fail to be reproduced correctly, if just 2BF is used. This deficiency can be resolved by inclusion of a TBF in the nuclear Hamiltonian. To avoid the full three-body problem, the TBF (semiphenomenological UIX interaction) is included via an effective two-body potential derived after averaging out the third particle, which is weighted by the LOCV two-body correlation functions $f_\alpha^p(ij)$ at a given density ρ_B. For more details, see Refs. [53,54].

2. Beta-stable matter

As the density of hadronic matter increases beyond the saturation density, nuclei dissolve to form an interacting system of nucleons and leptons. If this system survives longer than the timescale of weak interactions, $t \approx 10^{-10}$ s, it is able to reach equilibrium with respect to the β decay $n = p + e + \nu_e^-$ and its inverse, which is called beta-stable matter. Therefore, we have to consider the NS as an object of which the matter contains neutrons, protons, electrons, and muons. The τ lepton is ignored because of its large rest mass compared with two other leptons. For such matter, the β equilibrium conditions (without trapped neutrinos) are

$$\mu_n = \mu_p + \mu_e \quad (12)$$

$$\mu_e = \mu_\mu, \quad (13)$$

where μ_i stands for the chemical potential of each particle. Chemical potentials of leptons at zero temperature can be expressed as

$$\mu_i = \sqrt{(p_{Fi}c)^2 + (m_i c^2)^2}. \quad (14)$$

The charge neutrality condition in the NS matter requires the following equality:

$$\rho_p = \rho_\mu + \rho_e. \quad (15)$$

Solving the coupled equations (12), (13), and (15) self-consistently at any given baryon density ($\rho_B = \rho_n + \rho_p$), the energy of β-stable matter, which is written as the sum of the baryonic part energy E_B and leptonic part energy E_L, can be determined, ($E = E_B + E_L$). The energy of the baryonic part is calculated using Eq. (6). Leptons are supposed to be noninteracting highly relativistic particles, so at zero temperature, the energy of leptonic part can be written as

$$E_L = \frac{2}{h^3\rho_B}\sum_{i=e,\mu}\int_0^{P_{Fi}} d^3p_i\sqrt{(p_i c^2) + (m_i c^2)^2}. \quad (16)$$

The pressure of the NS matter as a function of baryonic density is calculated by using the following thermodynamic relation:

$$P = \rho_B^2\left(\frac{\partial(E/N)}{\partial\rho_B}\right). \quad (17)$$

B. Deconfined quark phase

Because of the nonperturbative and nonlinear nature of QCD, that is, governs the strongly interacting particles in the deconfined quark phase, describing such a system has

to be done via different models. In this study, we employ two well-known models, namely, the MIT bag model and the NJL model, which are briefly reviewed in the following subsections.

1. MIT bag model

An improved version of the MIT bag model in which interaction between u, d, and s quarks inside the bag are taken in a one-gluon-exchange approximation was employed [5,36–38]. At this stage, the thermodynamic potential (Ω) includes the quark kinetic energy, as well as one-gluon-exchange energy in which the fine structure constant of QCD is entered,

$$\Omega = \sum_f \Omega_f + B, \tag{18}$$

where B is the energy density difference between the perturbative vacuum and true vacuum, i.e., the bag constant which is the free parameter of the model, and at zero temperature Ω_f takes the form

$$\begin{aligned}\Omega_f(\mu_f) = \frac{-1}{4\pi^2}&\left[\mu_f\left(\mu_f^2 - \frac{5}{2}m_f^2\right)\sqrt{\mu_f^2 - m_f^2} + \frac{3}{2}m_f^4 \ln\left(\frac{\mu_f + \sqrt{\mu_f^2 - m_f^2}}{m_f}\right)\right] \\ &+ \frac{\alpha_c}{2\pi^3}\left[3\left(\mu_f\sqrt{\mu_f^2 - m_f^2} - m_f^2 \ln\left(\frac{\mu_f + \sqrt{\mu_f^2 - m_f^2}}{m_f}\right)\right)^2\right. \\ &- 2(\mu_f^2 - m_f^2)^2 - 3m_f^4 \ln\left(\frac{m_f}{\mu_f}\right) \\ &\left.+ 6\ln\frac{\sigma}{\mu_f}\left\{\mu_f m_f^2(\mu_f^2 - m_f^2)^{\frac{1}{2}} - \mu_f^4 \ln\left(\frac{\mu_f + \sqrt{\mu_f^2 - m_f^2}}{m_f}\right)\right\}\right],\end{aligned} \tag{19}$$

in which m_f and μ_f are the current quark mass and chemical potential, respectively, with $f = u,\ d,\ s$, and α_c denotes the QCD fine structure constant and $\sigma = \frac{m_N}{3} = 313$ MeV is the renormalization point, where m_N is the nucleonic mass. The masses of u and d quarks are neglected, and we take $m_s = 150,\ 300$ MeV. Thermodynamic quantities can be derived in the standard way:

$$n_f = \frac{\partial\Omega}{\partial\mu_f} \tag{20}$$

$$P = -\Omega \tag{21}$$

$$\epsilon = \Omega + \sum_f \mu_f n_f. \tag{22}$$

2. NJL model

We adopt the three-flavor version of the NJL model. The Lagrangian is given by [42]

$$L = \bar{q}(i\partial\!\!\!/ - \hat{m})q + L_{\text{sym}} + L_{\text{det}}, \tag{23}$$

$$L_{\text{sym}} = G\sum_{a=0}^{8}[(\bar{q}\lambda_a q)^2 + (\bar{q} + i\gamma_5\lambda_a q)^2] \tag{24}$$

$$L_{\text{det}} = -K[\det(\bar{q}(1+\gamma_5)q) + \det(\bar{q}(1-\gamma_5)q)], \tag{25}$$

in which $q = (u, d, s)^T$ is a quark field with three flavors ($N_f = 3$) and three colors ($N_c = 3$), and $\hat{m} = \text{diag}(m_u, m_d, m_s)$ is the corresponding quark mass matrix. As $m_s \neq m_u = m_d$, the isospin symmetery has been applied in this paper while SU(3) flavor symmetry explicitely broken. L_{sym} is a $U(3)_L * U(3)_R$ symmetric four-point interaction, in which λ_a, $a = 1, \ldots, 8$ denotes the Gell-Mann matrices, the generators of $SU(3)$. L_{det} concerns the 't Hooft interaction that is a $SU(3)_L * SU(3)_R$ symmetric $2N_f = 6$-point interaction, but it breaks the $U(1)$ symmetry, which was left unbroken by L_{sym}. G is the four-point coupling constant, and K is the six-point coupling constant. In the Hartree-Fock approximation, the quark self-energy, which arises from the interaction terms, is local and only implies a constant shift in the quark mass, which leads to the gap equation in the NJL model that is the relation between the constituent quark mass M and the current quark mass m [42],

$$M_i = m_i - 4G\varphi_i + 2K\varphi_j\varphi_k, \tag{26}$$

where (i, j, k) is equal to any permutation of (u, d, s) and $\varphi_i = \langle\bar{q}_i q_i\rangle$ is the quark condensate. NJL is a

TABLE I. Three parameter sets and related quark and meson properties in the three-flavor NJL model.

	RKH [78]	HK [39]	LKW [79]	Empirical [80]
Λ_c (MeV)	602.3	631.4	750	
$G\Lambda_c^2$	1.835	1.835	1.82	
$K\Lambda_c^5$	12.36	9.29	8.9	
$m_{u,d}$ (MeV)	5.5	5.5	3.6	3.5–7.5
m_s (MeV)	140.7	135.7	87	110–210
G_V/G	⋯	⋯	1.1	
f_π (MeV)	92.4	93.0	93	92.4
m_π (MeV)	135.0	138	139	135.0, 139.6
m_K (MeV)	497.7	496	498	493.7, 497.7
m_η (MeV)	514.8	487	519	547.3
$m_{\eta'}$ (MeV)	957.8	958	963	957.8
$m_{\rho,\omega}$ (MeV)	⋯	⋯	765	771.1, 782.6
m_{K^*} (MeV)	⋯	⋯	864	891.7, 896.1
m_ϕ (MeV)	⋯	⋯	997	1019.5

nonrenormalizable model, since there are divergent integrals in it, so there are different regularization schemes to regularize the divergencies, which are part of the NJL model. In this paper, the regularization has been done by using a sharp 3-momentum cutoff, Λ_c. There are five parameters that should be fixed in the $SU(3)$ NJL model: cutoff Λ_c; the bare quark mass $m_u = m_d$, m_s; and the coupling constants G and K. The parameters are fixed by fitting to the empirical values of five observables, namely, the pion decay constant f_π, the pion mass m_π, and the mass of three pseudoscalar mesons $k, \eta\, a, \acute{\eta}$. In Table I [42], we list three different parameter sets, which correspond to the fits of Rehberg, Klevansky, and Hufner (RKH) [78], of Hatsuda and Kunihiro (HK) [39], and of Lutz, Klimt, and Weise (LKW) [79], together with related quantities in the quark and meson sectors and their empirical values [80]. The empirical quark masses listed have been rescaled to a renormalization scale of 1 GeV by multiplying them by 1.35. The values given for the light quarks correspond to the average $(m_u + m_d)/2$. In RKH and HK parameter sets the parameters were determined by fitting f_π, m_π, m_k, and $m_{\acute{\eta}}$ to their empirical values, while the mass of the η meson is underestimated by 6% in the work of RKH and 11% in the work of HK. In the LKW parametrization, a vector and axial-vector interaction term is considered in addition to Eqs. (25) and (26) which enables the authors of ref [79] to fit the vector-meson nonet $(\rho, \omega, K^*$, and $\phi)$ as well, that cause LKW parameter set has a relatively large cut-off and small bare quark masses in comparison with RKH and HK parameter sets. In the pseudoscalar meson sector, all three parameter sets obtained similar results. In this paper, the numerical calculations have been done in all three RKH, HK and LKW parameter sets.

The mean field thermodynamics potential in the presence of the quark condensates at zero temperature takes the form [42]

$$\Omega(\mu_f, \varphi_f) = \sum_{f=u,d,s} \Omega_{M_f}(\mu_f) + 2G(\varphi_u^2 + \varphi_d^2 + \varphi_s^2) - 4k\varphi_u\varphi_d\varphi_s + \Omega_0, \tag{27}$$

where Ω_{M_f} corresponds to the contribution of a gas of a quasiparticle with mass M_f, which at zero temperature is written as

$$\Omega_{M_f}(\mu_f) = \frac{-N_c}{\pi^2}\int_{p_{F,f}}^{\Lambda} E_{p,f}p^2dp - \mu_f n_f, \tag{28}$$

in which $E_{p,f} = \sqrt{p^2 + M_f^2}$, $p_{F,f} = \sqrt{\mu_f^2 - M_f^2}$, and $n_f = \frac{(p_{F,f})^3}{\pi^2}$ are the on-shell energy, the Fermi momentum, and number density of a quark of flavor f with the constituent mass M_f and 3-momentum p, respectively. The thermodynamically consistent solutions correspond to the stationary point of Ω, which is found by minimizing it with respect to the condensates φ_u, φ_d, and φ_s $(\frac{\delta\Omega}{\delta\varphi_f} = 0)$. By applying the chain rule $(\frac{\delta\Omega}{\delta\varphi_f} = \frac{\partial\Omega}{\partial M_f}\frac{\delta M_f}{\delta\varphi_f}\frac{\partial\Omega}{\partial\varphi_f} = 0)$ and using Eqs. (26), (27), and (28), one finds φ_f given by

$$\varphi_f = \frac{-N_c}{\pi^2}\int_{p_{F,f}}^{\Lambda}\frac{M_f}{E_{p,f}}p^2dp. \tag{29}$$

φ_f has to be evaluated self-consistently with Eq. (26) and form a set of three coupled gap equations for the constituent quark masses. Ω_0 in Eq. (27) is chosen such that the thermodynamic potential Ω vanishes at zero μ and T.

Once the solutions of the gap equations for the constituent masses are found, other thermodynamic quantities can be derived in the standard way:

$$P = -\Omega, \qquad \epsilon = \Omega + \sum_f \mu_f n_f. \tag{30}$$

The weak decays $(d \leftrightarrow u + e + \bar{\nu}_e \leftrightarrow s)$ should be taken into account in the quark matter, so we have to include electrons (neutrinos have enough time to leave the system). The electrons are described by a noninteracting gas of massless fermions as often:

$$P_e = \frac{\mu_e^4}{12\pi^2} \rightarrow \epsilon_e = \frac{\mu_e^4}{4\pi^2}. \tag{31}$$

Therefore, we will have

$$P_{\rm tot} = P + P_e, \qquad \epsilon_{\rm tot} = \epsilon + \epsilon_e. \tag{32}$$

in the β-stable quark matter. The relations between chemical potentials of the particles take the form

$$\mu_d = \mu_s = \mu$$
$$\mu = \mu_u + \mu_e. \tag{33}$$

The charge neutrality condition implies $(\frac{2}{3}n_u - \frac{1}{3}n_d - \frac{1}{3}n_s - n_e = 0)$; thus, the system can be characterized by one independent variable, that is, the baryon number density $\rho_B = \frac{1}{3}(n_u + n_d + n_s)$.

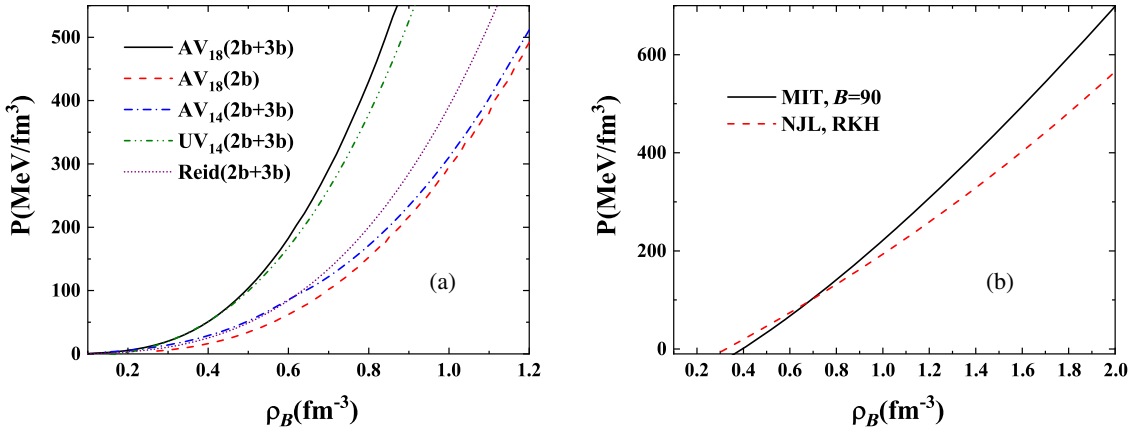

FIG. 1. (a) [(b)]: Pressure vs baryon number density for nuclear [quark] β-stable matter within the LOCV method for various interactions [NJL model in parameter set by RKH and the MIT model with $m_s = 150$ MeV and $B = 90$ MeV fm^{-3}].

III. RESULTS

Before starting to present the results for HSs, we show the EOS of pure hadronic and quark matter in Figs. 1(a) and 1(b). In Fig. 1(a). the pressures of nuclear β-stable matter vs baryon number densities, ρ_B, for various interactions are plotted. As seen in Fig 1. the EOS of the AV_{18} supplemented by TBF is stiffer with respect to the others, so the higher maximum mass is expected in comparison to the other EOS in the figure. In Fig. 1(b). the pure quark matter pressure vs baryon number density is

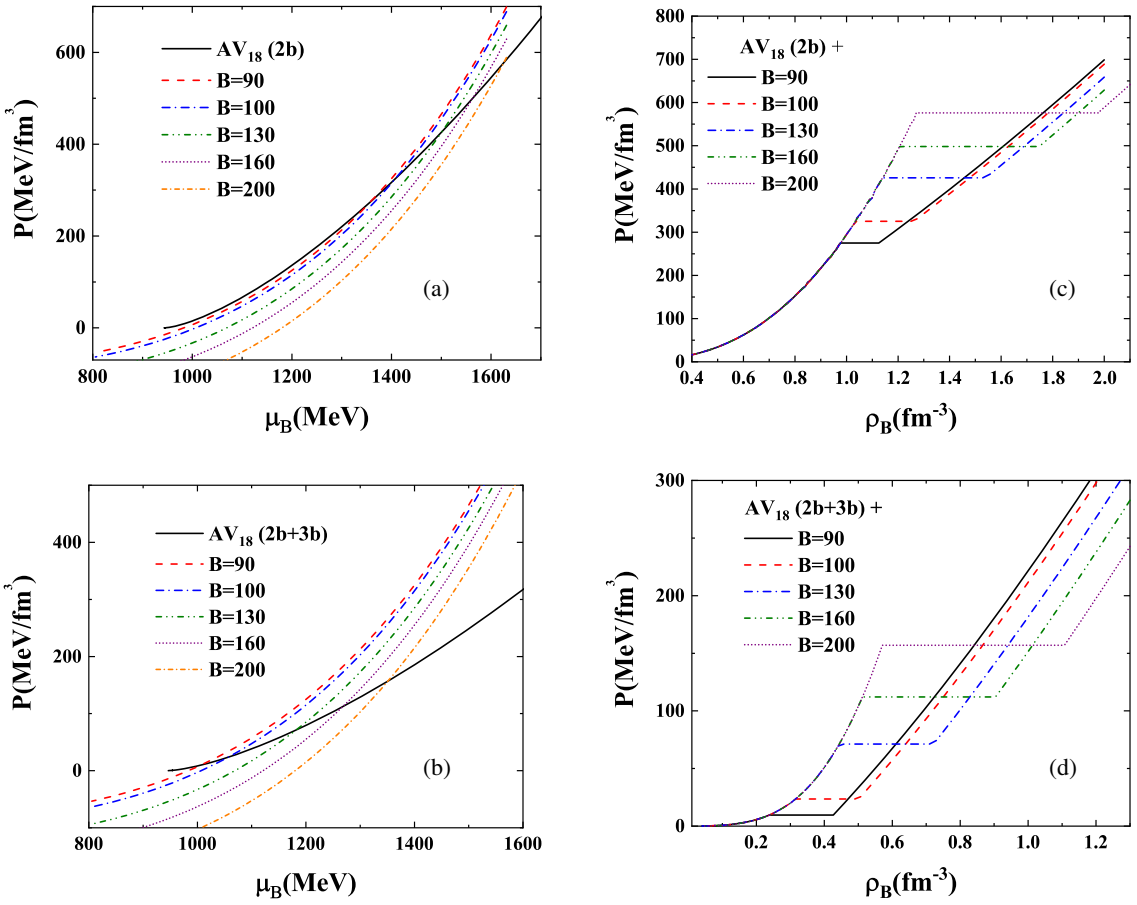

FIG. 2. (a) [(b)]: Pressure vs baryon chemical potential for the MIT model with $m_s = 150$ MeV and various bag constants and AV_{18} interaction supplemented without [with] TBF. (c) [(d)]: The corresponding hadron-quark hybrid EOS in Maxwell construction without [with] TBF.

plotted for a sample parameter of the MIT bag model with $B = 90$ MeV fm^{-3} and the NJL model with the RKH parameter set. Our calculation is in line with the original calculations in Refs. [37,42].

A. Hadron-quark hybrid EOS

To establish that an EOS governs to whole HS, one needs to investigate the hadron-quark phase transition. As the quark-hadron mixed phase is unlikely to be stable for reasonable values of the surface tension [58–60], we restrict ourselves to analyzing the phase transition on Maxwell construction that is a sharp phase transition from neutral hadronic matter to homogeneous neutral quark matter. Each phase is considered to be in β equilibrium and also charge neutrality. The requirement of the charge neutrality effectively reduces each phase to a one-component system controlled by the baryonic density or equivalently a baryonic chemical potential. The transition point in the Maxwell construction is identified by the conditions of thermal, mechanical and one-component chemical equilibrium, which at zero temperature takes the form

$$P_1(\mu_B) = P_2(\mu_B), \tag{34}$$

in which subscript 1 (2) stands for the hadronic (quark) phase. Equation (34) means that Maxwell construction corresponds to constant pressure in the density interval between two phases. μ_B is the baryon chemical potential ($\mu_{B1} = \mu_p + \mu_n$ and $\mu_{B2} = \mu_u + \mu_d + \mu_s$). This equation also means that in this construction the baryon chemical potential μ_B is continuous, whereas the electron chemical potential μ_e jumps at the interface between the two phases (in Gibbs construction, the electron chemical potential is taken as continuous, too [5]). Maxwell construction can be considered as a limiting scenario in which the surface tension is large.

1. MIT bag model

We will first discuss the results obtained with the MIT bag model with a strange rest mass of $m_s = 150$ MeV for the quark sector. In Fig. 2(a) [2(b)], we plot the pressure as a function of baryonic chemical potential in the MIT bag model with various bag constants and the LOCV method with AV_{18} interaction supplemented without (with) TBF, respectively. In Figs. 2(c) [2(d)] the corresponding hybrid star EOS are displayed in Maxwell construction. For the bag constant less than 78 MeV fm^{-3}, there is no intersection between the hadron and quark pressure curves, which means the nucleonic phase will remain stable with respect to the formation of quark phase droplets for noted bag constants. For 78 MeV fm^{-3} $\leq B \leq$ 84 MeV fm^{-3}, the hadron transition densities are less than nuclear saturation density, ρ_0. Thus, we focus on the phase transition for $B \geq 90$ MeV fm^{-3}, in which the transition densities are

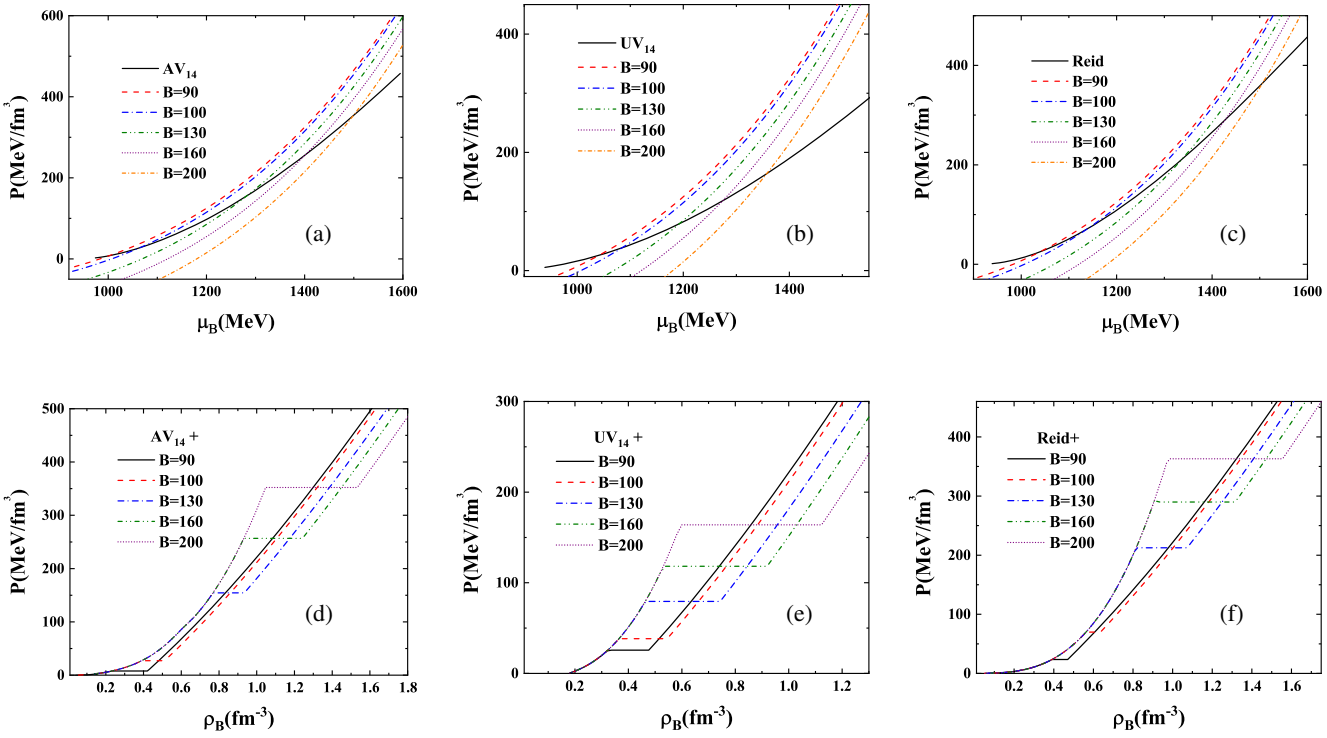

FIG. 3. (a), (b), and (c) : Pressure vs. baryon chemical potential for MIT bag model with various bag constants and $m_s = 150$ MeV combined with AV_{14} , UV_{14} and Reid 68 interactions supplemented by TBF respectively. (d), (e), and (f) : The corresponding hadron-quark hybrid EoS's in Maxwell construction with AV_{14} , UV_{14} and Reid 68 interactions supplemented by TBF.

more than $1.5\rho_0$. As the bag constant increases, the phase transitions from nuclear to quark matter take place at rather high baryon densities, and also the transition region extends. When we consider just 2BF, the EOS becomes much softer, and the phase transitions take place in much higher densities. In this case, the phase transition occurs in about $6\rho_0$ with $B = 90$ MeV fm^{-3}.

To examine the effect of nucleon-nucleon (N-N) interactions on the hadron-quark phase transition region, we have also carried out the calculations with some other bare two-body N-N interactions supplemented with TBF, namely, AV_{14}, UV_{14}, and Reid 68, the results of which are displayed in Fig. 3. In Figs. 3(a), 3(b), and 3(c), we display quark matter EOS in the MIT bag model with various bag constants and hadronic matter EOS with AV_{14}, UV_{14}, and Reid 68 potential, respectively. In Figs. 3(d), 3(e), and 3(f), the corresponding hybrid EOS are displayed. The transition densities in these cases are almost in similar ranges. Again, the phase transition moves to high baryon densities, and the transition region extends as the bag constant increases.

The hadron-quark phase transition properties for various N-N interactions and bag constants are summarized in Table II, in which it is seen that the range of critical baryon chemical potential is almost similar in all hadron interactions supplemented by the TBF. We further observe that they are lower than the situation in which the TBF is not considered. In the latter, increasing the critical chemical potential increases the critical baryon density and also extends the transition region. As seen in Table II, in this situation, we observe high-energy density discontinuity in comparison with considering the TBF in any bag constants. In all hadron interaction supplemented by TBF with $B = 90, 100$ MeV fm^{-3}, the energy discontinuity is around 200 MeV fm^{-3}, while in the cases $B = 130, 160, 200$ MeV fm^{-3}, the energy density discontinuities takes larger values. If the energy density discontinuity becomes too high, then the star becomes unstable as soon as the quark matter core appears, which itself is due to the fact that the pressure of the quark matter is unable to cancel out the additional downward force from the gravitational attraction that the additional energy in the core applies on the rest of the star (we will elaborate on this point in Sec. III B 1).

2. NJL model

Now, we present the numerical results for the NJL model for the quark matter sector. In Figs. 4(a), 4(b), and 4(c), we

TABLE II. Hadron-quark phase transition properties for various N-N interactions and various bag constants with $m_s = 150$ MeV, where μ_B is the critical baryon chemical potential, ρ_B/ρ_0 is the ratio of baryon density to the saturation density, and ϵ is the energy density at starting point (1) and ending point (2) of the phase transition.

Hadron interaction	Bag constant (MeV fm^{-3})	μ_B (MeV)	$\rho_B^{(1)}/\rho_0$	$\rho_B^{(2)}/\rho_0$	$\epsilon^{(1)}$ (MeV fm^{-3})	$\epsilon^{(2)}$ (MeV fm^{-3})
AV_{18} (2BF)	90	1358.1	6.06	7	1051.5	1253.4
	100	1407.94	6.43	7.87	1130.6	1450.5
	130	1500.2	7.12	9.62	1284.3	1884.7
	160	1561.9	7.5	10.93	1385.4	2231.5
	200	1624.6	7.93	12.31	1488.6	2634.0
AV_{18} (2BF + 3BF)	90	1006.0	1.5	2.68	229.8	419.4
	100	1056.4	2	3.12	309.6	505.8
	130	1181.7	2.75	4.5	453.2	781.5
	160	1207.7	3.18	5.62	537.4	1033.8
	200	1351	3.56	6.87	614.4	1338.7
AV_{14}	90	1001.8	1.43	2.62	224.6	413.5
	100	1003.2	2.43	3.18	387.3	516.92
	130	1281.0	4.81	5.81	830.0	1042.6
	160	1401.3	5.81	7.75	1048.9	1484.6
	200	1448.0	6.5	8.43	1216.13	1944.9
UV_{14}	90	1040.7	2.12	2.93	332.2	470.7
	100	1084.0	2.31	3.37	375.2	552.7
	130	1192.7	2.93	5.83	486.0	807.2
	160	1274.3	3.37	5.75	567.3	1053.1
	200	1357.2	3.75	7	647.1	1360.1
Reid 68	90	1036.3	2.43	2.93	316.4	463.9
	100	1136.5	3.5	3.93	593.1	652.9
	130	1337.9	5.06	6.68	877.7	1223.4
	160	1426.9	5.75	8.18	1029.6	1587.4
	200	1504.9	6.18	9.68	1126.4	1977.5

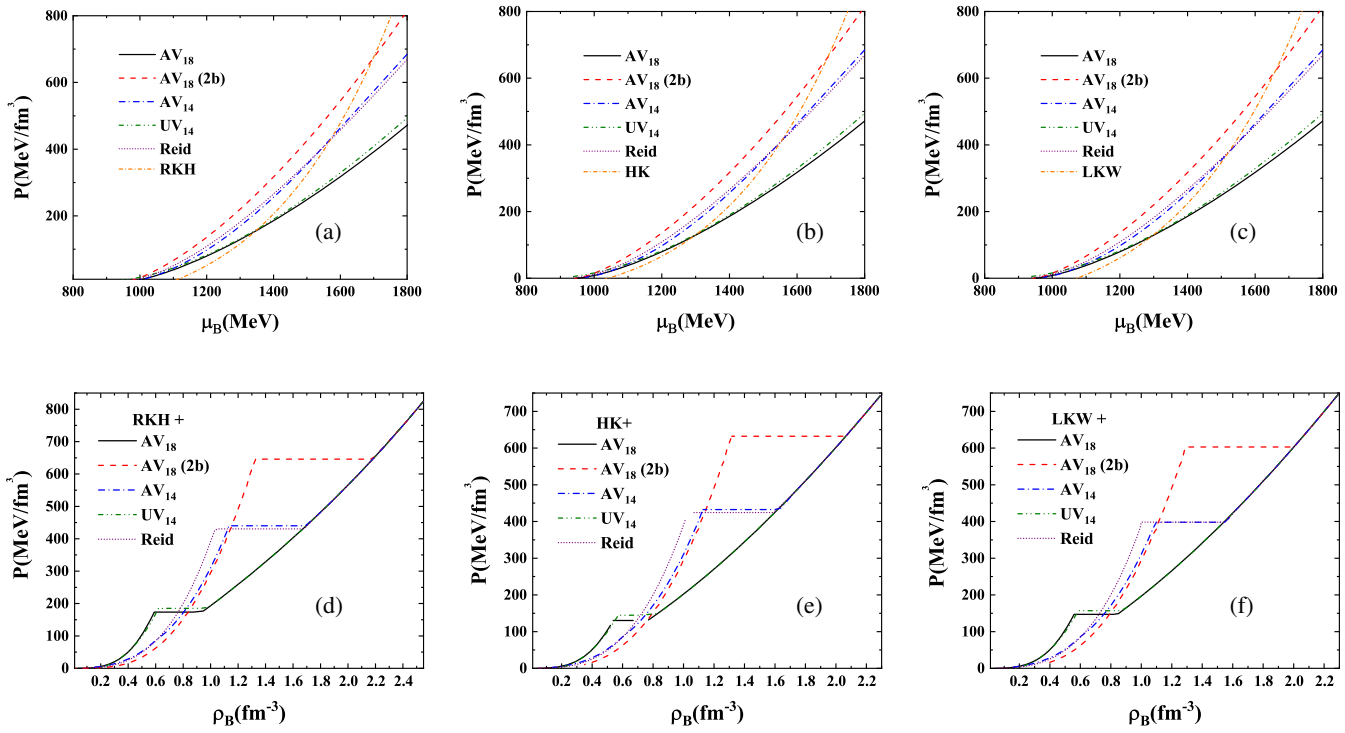

FIG. 4. (a), (b), and (c): Pressure vs baryon chemical potential for various hadron interactions combined with NJL in RKH, HK, and LKW parameter sets, respectively. (d), (e), and (f): The corresponding hadron-quark hybrid EOS in Maxwell construction with NJL in RKH, HK, and LKW parameter sets.

display the pressure vs baryon chemical potential of the hadronic matter EOS with various hadron interactions and quark matter EOS within the NJL model for RKH, HK, and LKW parameter sets, respectively, whereas Figs. 4(d), 4(e), and 4(f) are the corresponding hybrid EOS. It is worth noting that in all above cases the phase transition occurs. In the RKH parameter set, the transition density occurs in a little higher chemical potential than the cases in the HK and LKW parameter sets for all hadronic EOS. By using only two-body N-N potential, the phase transition density occurs in considerably large densities compared with considering the three-body forces in all potentials, for any three parameter sets. Here, the starting point of the phase transition occurs in about $7\rho_0$, but with TBF, it occurs in slightly more than $3\rho_0$ with AV_{18} combined with TBF.

Table III summarizes the hadron-quark phase transition properties for various N-N interactions and various parameter sets of the NJL model. As seen in this table, and in comparison with Table II, when we use the NJL as the quark model, the values of critical chemical potentials increase relative to the MIT bag model with the same hadron interactions and correspond to large values of the bag constant. With the increasing the chemical potential, the critical baryon density rises, and the phase transition region extends, which enlarges the energy discontinuity for any parameter sets. Except for the HK parameter set combined with the AV_{18} and UV_{14} supplemented by TBF for which the energy discontinuity is lower than around 200 MeV fm^{-3}, in the other hadron interactions with and without TBF, the energy discontinuities are around 400–1300 MeV fm^{-3}, and these values are too large to retain the stability of the star. As we mentioned earlier, if the energy density discontinuity becomes considerably too high, the star becomes unstable. Since the pressure of the quark matter is unable to counteract the additional downward force from the gravitational attraction (we will refer to this point in Sec. III B 2).

B. Hybrid star structure

The structure of a hybrid star is calculated by numerical integration of the Tolman-Oppenheimer-Volkoff (TOV) equations

$$\frac{dP(r)}{dr} = -\frac{GM(r)\epsilon(r)}{c^2r^2}\left(1+\frac{P(r)}{\epsilon(r)}\right)\left(1+\frac{4\pi r^3P(r)}{M(r)c^2}\right) \times \left(1-\frac{2GM(r)}{rc^2}\right)^{-1}, \tag{35}$$

$$\frac{dM(r)}{dr} = \frac{4\pi\epsilon(r)r^2}{c^2}, \tag{36}$$

in which $\epsilon(r)$ is the total energy density, $M(r)$ is the star mass within radius r, and G denotes the gravitational constant.

TABLE III. Same as Table. II but with the NJL model in various parameter sets for the quark phase.

Hadron interaction	NJL	μ_B (MeV)	$\rho_B^{(1)}/\rho_0$	$\rho_B^{(2)}/\rho_0$	$\epsilon^{(1)}$ (MeV fm^{-3})	$\epsilon^{(2)}$ (MeV fm^{-3})
AV_{18} (2BF)	RKH	1678.5	8.25	13.62	1583.9	2947.6
	HK	1668.1	8.18	12.75	1561.1	2780.3
	LKW	1645.6	8	12.5	1516.5	2703.0
AV_{18} (2BF + TBF)	RKH	1379.7	3.68	5.43	640.5	1039.76
	HK	1302.9	3.31	4.12	570.10	742.4
	LKW	1333.6	3.43	5.12	598.10	941.8
AV_{14}	RKH	1578.83	7.06	10.56	1349.5	2355.3
	HK	1572.0	7	10.18	1338.6	2255.8
	LKW	1540.9	6.8	9.68	1288.6	2080.9
UV_{14}	RKH	1392.8	4.12	5.81	739.1	1112.9
	HK	1323.8	3.56	4.37	614.5	789.2
	LKW	1345.5	3.68	5.31	635.7	993.8
Reid 68	RKH	1573.5	6.63	10.5	1241.6	2320.2
	HK	1567.2	6.62	9.93	1238.9	2223.3
	LKW	1540.9	6.25	9.62	1145.3	2080.7

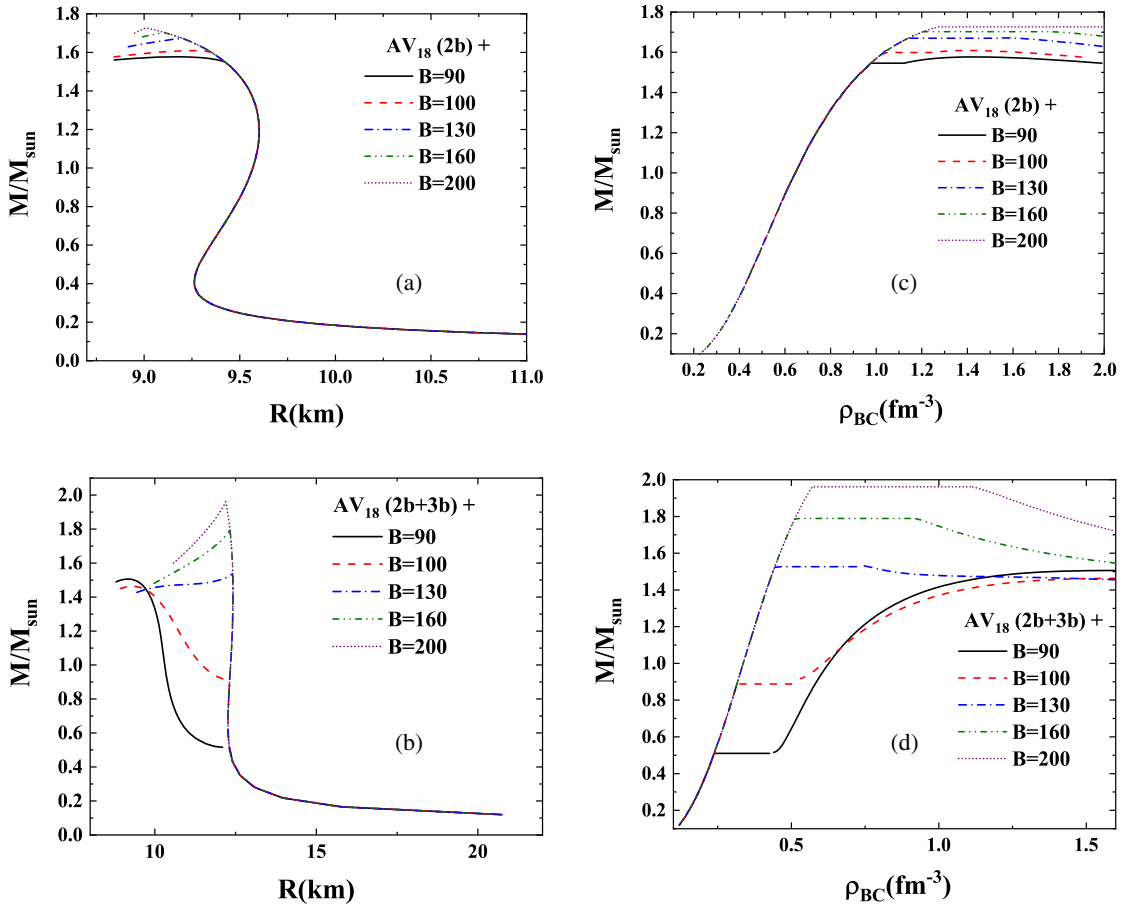

FIG. 5. (a) [(b)]: The gravitational HS masses vs radius of the star for the MIT bag model with various bag constants and $m_s = 150$ MeV combined with AV_{18} interaction supplemented without [with] TBF. (c) [(d)]: The corresponding gravitational HS mass vs central baryon density of the star without [with] TBF.

1. MIT bag model

First, the result of a HSs structure concerning the MIT bag as a quark model is presented. In Figs. 5(a) [5(b)], we plot the gravitational HS mass vs radius within the MIT bag model with $m_s = 150$ MeV and various bag constants, combined with AV_{18} interaction supplemented without [with] TBF and in Figs. 5(c) [5(d)], the corresponding gravitational HS mass vs central baryon density of the star, ρ_{BC}, are displayed. The results of other N-N interactions are displayed in Fig. 6. In Figs. 6(a), 6(b), and 6(c), we plot the mass radius relation for HSs within the MIT bag model with $m_s = 150$ and various bag constants combined with AV_{14}, UV_{14}, and Reid 68 interactions supplemented by TBF. In Figs. 6(d), 6(e), and 6(f), the corresponding gravitational HS mass vs central baryon density of the star is displayed.

Stable hybrid star with pure quark core is predicted with $B = 90, 100$ MeV fm^{-3} combined with all hadron interactions with or without TBF and also $B = 130$ MeV fm^{-3} combined with AV_{14} interaction supplemented by TBF. The strange mass is considered $m_s = 150$ Mev in above cases. As seen in Figs. 5 and 6, in these cases, the mass vs central baryon density curves are obviously increasing after the onset of the pure quarks in the core of the star, and also mass-radius curves are smooth at the maximum point. In other cases, although the mass vs central baryon density curves show a slight increasing behavior after the onset of pure quarks in the core through a small density range, there is a cusp at the maximum point in mass-radius curve in all of them. However, maybe it is not clearly visible in some cases, but since the central baryon density in which the maximum mass occurs is a little higher than transition density of a quark to a hadron, the curves continue to increase through a very small density range. The values of densities are comparable in Tables II and IV. As seen in Table II, in the cases of stable hybrid star with pure quark core, the energy density discontinuity is low, while in other cases in which the energy density discontinuity extend more, a stable HS with a pure quark core is not accessible. In the latter, the large energy discontinuity at the transition point is reflected as a cusps on the mass radius relation. These cusps are clearly visible in mass-radius curves of Figs. 5 and 6. The effects are strong enough to render the star unstable. The maximum mass of the stable HS with pure quark core is about 1.5 $M_\odot$ in all hadron interaction cases. For the HS with $B = 200$ MeV fm^{-3}, combined with AV_{18} interaction supplemented by TBF, however, the maximum mass reaches 1.962 which is compatible with the observations, the star becomes unstable as soon as the quark phase onset in the core of the star.

In Table IV, we summarize the structure properties of pure neutron and hybrid stars for various N-N interactions and bag constants of the MIT bag model with $m_s = 150$ MeV.

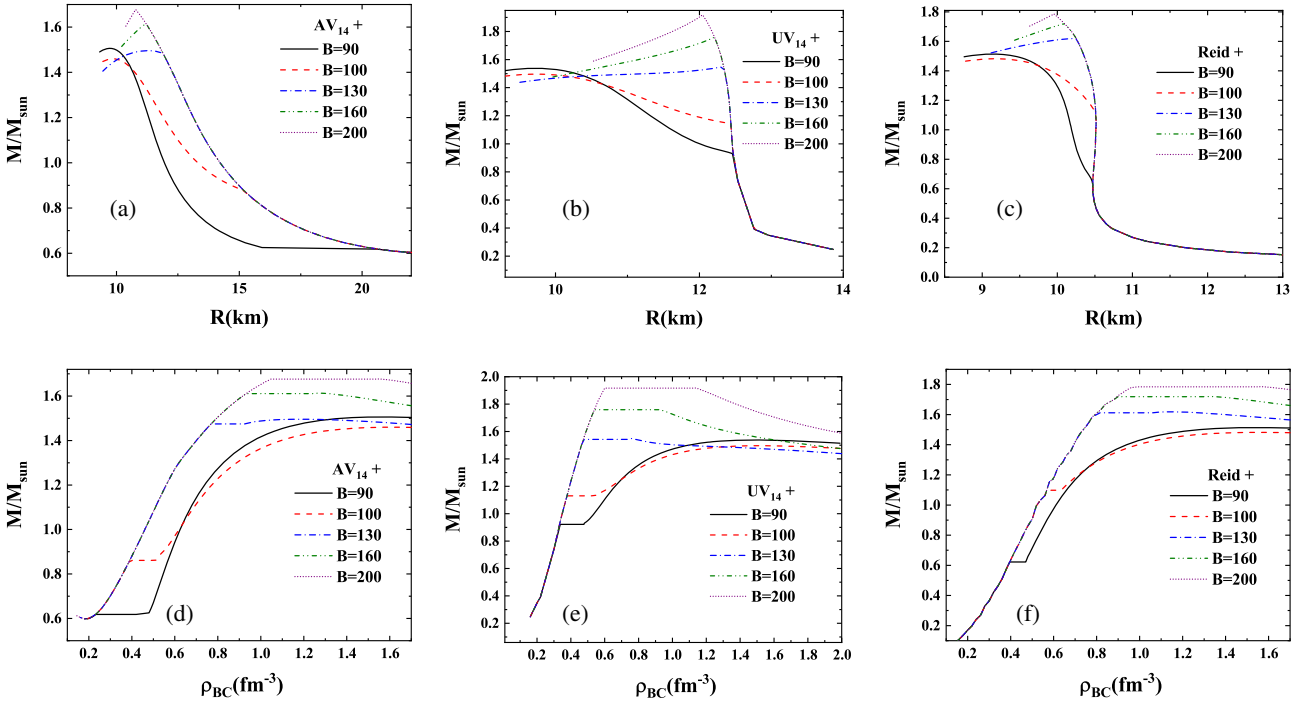

FIG. 6. (a), (b), and (c): The gravitational HS masses vs the radius of the star within the MIT bag model with various bag constants and $m_s = 150$ MeV combined with AV_{14}, UV_{14}, and Reid 68 hadron interactions supplemented by TBF, respectively. (d), (e), and (f): The corresponding gravitational HS mass vs central baryon density of the star with AV_{14}, UV_{14}, and Reid 68 hadron interactions supplemented by TBF.

TABLE IV. Pure NS and HS structure properties in which M_{max} ($M_\odot$) is the maximum mass of the star in the mass of the sun unit, $\rho_{BC\,max}$ is the central density, and R_{max} (Km) is the radius of the star according to the maximum mass of the star, for various hadron interactions and bag constants with $m_s = 150$ MeV.

Hadron interaction	Bag constant ($\frac{MeV}{fm^3}$)	$\rho_{BC\,max}$ (fm^{-3})	R_{max} (km)	M_{max} ($M_\odot$)
AV_{18} (2BF)	NS	1.62	8.5	1.77
	90	1.44	9.16	1.57
	100	1.40	9.25	1.61
HS ⇛	130	1.57	9.19	1.67
	160	1.76	9.10	1.70
	200	1.98	9.00	1.72
AV_{18} (2BF + TBF)	NS	0.94	10.95	2.319
	90	1.57	9.16	1.50
	100	1.63	9.81	1.46
HS ⇛	130	0.73	12.4	1.53
	160	1.27	11.2	1.609
	200	1.11	12.19	1.962
AV_{14}	NS	1.53	9.59	1.76
	90	1.55	9.75	1.5
	100	1.62	9.85	1.46
HS ⇛	130	1.19	11.27	1.49
	160	1.27	11.2	1.61
	200	1.54	10.79	1.67
UV_{14}	NS	1.00	10.76	2.24
	90	1.49	9.71	1.53
	100	1.51	9.73	1.49
HS ⇛	130	0.75	12.33	1.55
	160	0.92	12.21	1.76
	200	1.13	12.04	1.918
Reid 68	NS	1.44	9.15	1.91
	90	1.55	9.14	1.513
	100	1.56	9.17	1.48
HS ⇛	130	1.14	10.2	1.618
	160	1.33	10.09	1.719
	200	1.56	9.95	1.72

We examine the effect of increasing the strange mass on the MIT model results, which are displayed in Fig. 7. In Figs. 7(a), 7(b), and 7(c), we display pressure vs baryon density in Maxwell construction, mass vs radius, and mass vs central density of HSs for the bag constant of $B = 90$ MeV fm^{-3} with $m_s = 300$ MeV combined with several hadron interactions with or without TBF. As seen in Fig. 7(a), AV_{18} and UV_{14} potentials supplemented by TBF have almost the same phase transition densities, while in AV_{14} and Reid potentials supplemented by TBF, these values are higher than them. In the case with just considering 2BF, the phase transitions take place in much higher densities. As seen in Figs. 7(c) and 7(b), the stable HS is predicted with AV_{18} and UV_{14} potentials supplemented by TBF with the maximum masses of 1.796 $M_\odot$ and 1.778 $M_\odot$ respectively, since the gravitational mass continues to increase after the onset of the quark, and also the maximum point in the mass-radius curve is stiff. The situation is better with respect to the results gained in the case with $m_s = 150$ MeV in which the predicted stable HSs reach the maximum mass of about 1.5 $M_\odot$. The other HSs are predicted to be unstable because of the appearance of cusps in mass-radius curves, which render the star unstable. In Figs. 7(d), 7(e), and 7(f), we examine the effect of increasing the bag constant on the results. As seen in Fig. 7(d), as the bag constant increases, the phase transitions take place at rather high baryon densities, and also the transition region extends, which corresponds to the unstable HS since As seen in Fig. 7(e), there are cusps in mass radius curves which rendered the star unstable in mentioned cases. Nevertheless, the maximum masses of 2.05 $M_\odot$ and 2.13 $M_\odot$ are calculated for $B = 160$ MeV fm^{-3} and $B = 200$ MeV fm^{-3} combined with AV_{18} potential supplemented by TBF.

The results of phase transition and the HS structure of the mentioned model are summarized in Tables V and VI. By looking at Table V, one can realize that the energy density discontinuity in AV_{18} and UV_{14} potentials supplemented by TBF is very low, around 100 MeV fm^{-3}, while in other cases, this value is higher, and again we conclude that high-energy density discontinuity is responsible for the instability of HSs.

Our results are in line with other works in HSs with other hadronic EOS such as the microscopic Brueckner-Hartree-Fock (BHF) many-body theory, relativistic mean field (RMF) model [5,81,82], APR98 variational chain summation method, and also Valecka models [83]; all these EOS are combined with the MIT bag model in which HSs with bag constants of around $B = 90$ MeV fm^{-3} and $m_s = 150$ MeV fm^{-3} are stable with a pure quark core and the maximum mass is about 1.5 $M_\odot$. It is to be noted that for a large bag constant, bigger than around $B = 140$ MeV fm^{-3}, the stability of the star will be lost.

2. NJL model

In this subsection, we will present the results of the HS structure within the NJL model. In Figs. 7(a), 7(b), and 7(c), we plot the HS gravitational mass vs radius of the star for various hadronic interactions and RKH, HK, and LKW parameter sets, respectively, and Figs. 7(d), 7(e), and 7(f) show the corresponding HS mass vs central baryon density of the star. In all cases, the maximum masses of HSs are more than 1.693 $M_\odot$. In the RKH parameter set with AV_{18} combined with TBF, it reaches 2.01 $M_\odot$. As seen in Fig. 8(b) in the HSs within the HK parameter set combined with AV_{18} and UV_{14} interactions, the cusps in mass-radius relations are slightly smoothed out and therefore the corresponding HSs are stable. As seen in Fig. 8(e) the

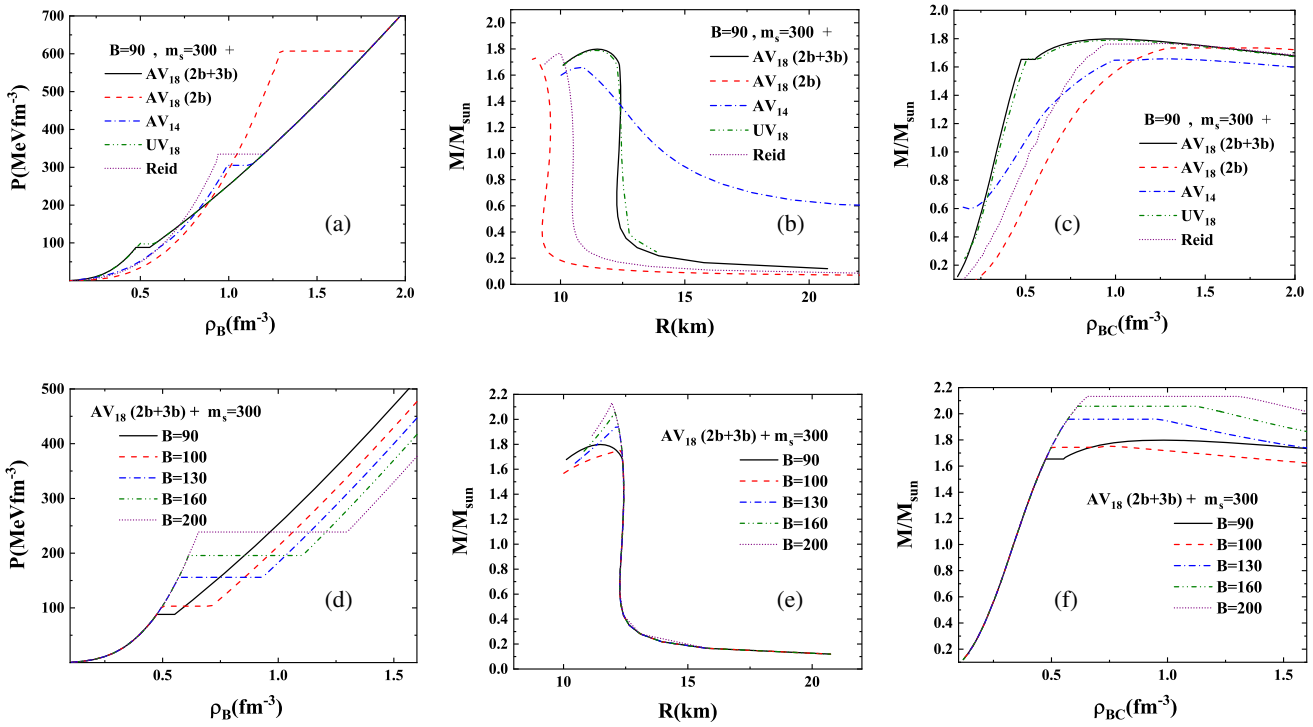

FIG. 7. (a)–(c): Pressure vs baryon density, the gravitational HS masses vs radius, and central baryon density of the stars for various hadronic interactions and the bag constant of $B = 90$ MeV fm^{-3} and $m_s = 300$ MeV, respectively. (d)–(f): The same as the previous panels but for AV_{18} interaction supplemented with TBF and various bag constants of the MIT bag model with $m_s = 300$ MeV.

mass-central density curves obviously increases after the onset of quark phase.

In other cases, although the curves increase slightly through a very small density range by the onset of the pure quark phase, in mass-radius curves, there exist cusps in maximum point which cause the instability of the HSs. However, maybe it is not clearly visible in some cases, but since the central baryon density in which the maximum mass occurs is a little higher than the transition density of a quark to a hadron, the curves continue to increase through a very small density range. The values of densities are comparable in Tables III and VII, which will be presented in following. In Table V, we summarize the structure properties of pure neutron and hybrid stars for various hadron interactions and parameter sets of the NJL model.

In all cases, the energy density discontinuity in transition region is large enough to make a cusp in mass-radius curves. The only exception is HK parameter set combined with AV_{18} and UV_{14} interactions combined with TBF. It turns out, however, that in these cases the cusps are so strong that the stars are rendered unstable. In the HK parameter set with AV_{18} and UV_{14} supplemented by TBF, the cusps are slightly smoothed out, and the corresponding HSs are stable. The results in both quark models lead to the

TABLE V. Same as Table. II but with $m_s = 300$ Mev.

Hadron interaction	Bag constant (MeV fm^{-3})	μ_B (MeV)	$\rho_B^{(1)}/\rho_0$	$\rho_B^{(2)}/\rho_0$	$\epsilon^{(1)}$ (MeV fm^{-3})	$\epsilon^{(2)}$ (MeV fm^{-3})
AV_{18} (2BF)	90	1648	8.05	11.16	1519.86	2338.4
AV_{18} (2BF + 3BF)	90	1218.9	2.96	3.45	490.4	584.9
AV_{14}	90	1451	6.2	7	1137.0	1331.6
UV_{14}	90	1232.3	3.16	3.62	525.9	617.5
Reid	90	1475	5.82	7.48	1053.7	1431.5
AV_{18} (2BF + 3BF)	100	1250.0	3.11	4.43	520.19	787.1
	130	1349.3	3.55	5.82	612.7	1102.3
	160	1416.7	3.82	6.5	672.5	1369.4
	200	1484.9	4.09	8.114	734.09	1689.3

TABLE VI. Same as Table IV but with $m_s = 300$ MeV.

Hadron interaction	Bag constant $(\frac{\text{MeV}}{\text{fm}^3})$	$\rho_{BC\,\max}$ (fm^{-3})	$R_{\max}$ (km)	$M_{\max}$ $(M_\odot)$
AV_{18} (2BF)	90	1.79	8.97	1.73
AV_{18} (2BF + TBF)	90	0.92	11.59	1.796
AV_{14}	90	1.27	10.8	1.65
UV_{14}	90	1.57	9.19	1.67
Reid 68	90	0.99	11.43	1.788
AV_{18} (2BF + TBF)	100	0.74	12.31	1.75
	130	0.94	12.19	1.96
	160	1.104	12.07	2.05
	200	1.298	11.94	2.13

point that considerably larger energy densities in the quark core probably are the driving factor for the instability.

Our results are in acceptable concurrence with those of some works conducted in HSs within the original NJL model and other hadron models [27,33,42,84–86]. According to the conclusions of forgoing papers, other hadronic equations of state, namely, BHF many-body theory and also the RMF model combined with NJL, the stable HS with a pure quark core is not predictable. This result seems to be rather insensitive to the choice of the hadronic EOS and must mainly be attributed to the quark EOS derived within the NJL model [27,42,84]. In Ref. [27], the authors conclude that the instability is closely linked to the lack of confinement in the original NJL model. Besides, as is pointed out in Ref. [42], these results rely heavily on the assumption that the NJL model parameters which have been fitted in vacuum can be applied to dense matter. However, according to all the findings in HSs, it is also possible that applying the vacuum fitted parameters to dense matter is not the correct approach and maybe a considerable modification of the effective NJL-type quark interactions in dense matter is needed.

We close this subsection by displaying the energy density, pressure, and mass profiles of the HSs investigated in the paper for a sample central density of $\rho_{\text{cent}} = 1.03\ \text{fm}^{-3}$ in Fig. 9. For $m_s = 300$ MeV, we display the profiles only for a bag constant of $B = 90\ \text{MeV fm}^{-3}$. As seen in Figs. 9(a), 9(d), 9(g), 9(j), and (9)m, the energy density decreases from the center to the surface of the star, and in phase transition density, there is a sudden decreasing in the amount of energy density that is characteristic of Maxwell construction. As is clear in the figures, this energy discontinuity is obviously large in RKH and LKW parameter sets in the NJL model and also high bag constants of the MIT bag model, which, as we point out before, probably is the driving factor for the instability of corresponding HSs. Some of the energy density profiles do not have this discontinuity since the sample central density of

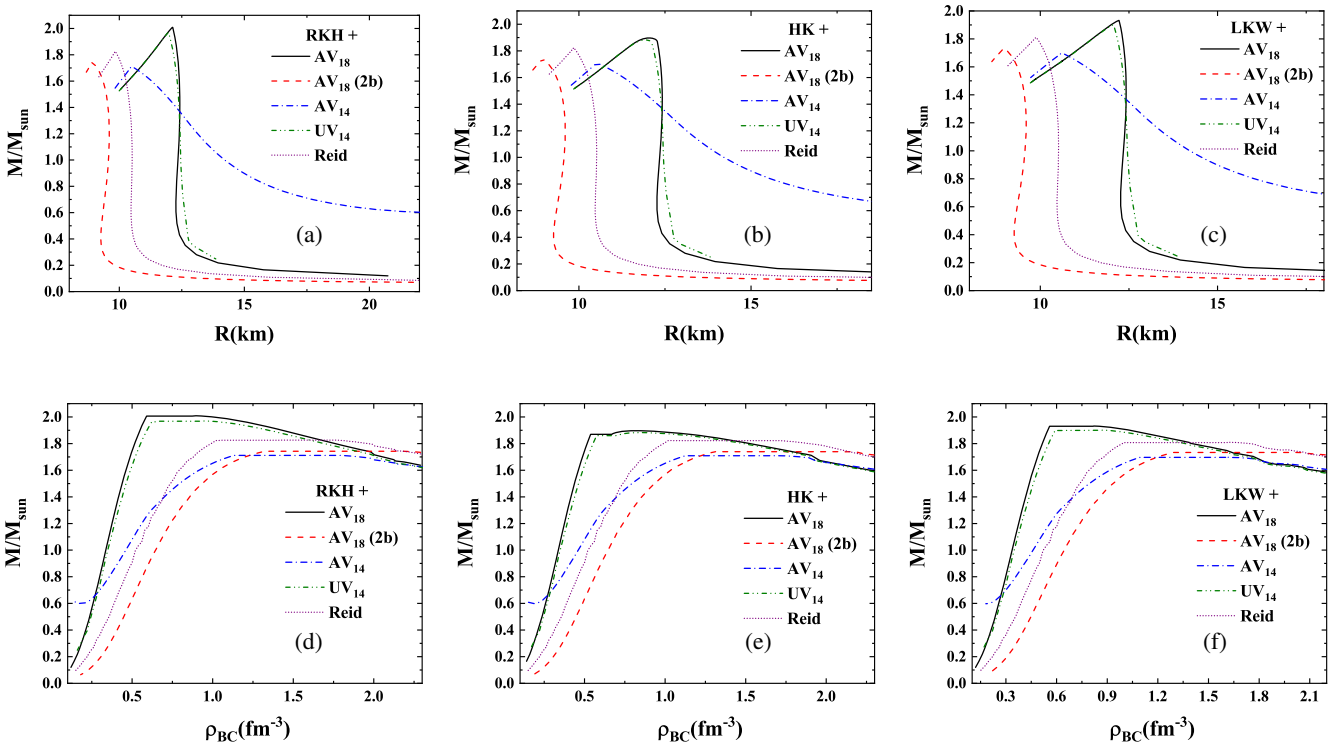

FIG. 8. (a), (b) , and (c): The gravitational HS masses vs radius of the star for various hadronic interactions and NJL with the RKH, HK, and LKW sets of parameters, respectively. (d), (e), and (f): The corresponding gravitational HS masses vs central baryon density of the star for RKH, HK, and LKW parameter sets.

TABLE VII. Same as Table. IV but with the NJL model with various parameter sets for the quark model.

Hadron interaction	NJL	$\rho_{BC\,\max}$ (fm^{-3})	$R_{\max}$ (km)	$M_{\max}$ ($M_\odot$)
AV_{18} (2BF)	NS	1.62	8.5	1.77
	RKH	2.15	8.92	1.74
Hs ⇛	HK	2.05	8.94	1.738
	LKW	2.01	8.97	1.73
AV_{18} (2BF + TBF)	NS	0.94	10.95	2.319
	RKH	0.89	12.13	2.009
HS ⇛	HK	0.82	12.03	1.896
	LKW	0.83	12.21	1.932
AV_{14}	NS	1.53	9.59	1.76
	RKH	1.77	10.49	1.77
Hs ⇛	HK	1.71	10.51	1.71
	LKW	1.61	10.60	1.69
UV_{14}	NS	1.00	10.76	2.24
	RKH	0.94	11.97	1.97
HS ⇛	HK	0.84	11.92	1.88
	LKW	0.87	12.06	1.90
Reid 68	NS	1.44	9.15	1.91
	RKH	1.76	9.83	1.82
HS ⇛	HK	1.69	9.84	1.822
	LKW	1.61	9.87	1.81

$\rho_{\mathrm{cent}} = 1.03\ \mathrm{fm}^{-3}$ for those HSs is lower than the transition density; therefore, the corresponding star is a purely hadron star. As seen in Figs. 9(b), 9(e), 9(h), 9(k), and 9(n), the pressure of star monotonically decreases from the center to the surface of the star, as we expected from the TOV equations. As seen in Figs. 9(c), 9(f), 9(i), 9(l), and 9(o), the mass of the star increases monotonically from zero at the center to the star mass at the surface of the star, as we expected from the TOV equations.

C. Tidal deformability

Gravitational waves from the final stage of inspiraling binary NSs are expected to be one of the most important sources for gravitational wave detectors. Large finite-size (tidal) effects are measurable toward the end of inspiral [87], but the gravitational wave signal is expected to be very complex during this period. Tidal effects during the early part of the evolution will form a very small correction, but during this phase, the signal is very clean [88]. The tidal fields induce quardupole moments on the NSs. This response of each star to the external disturbance is described by the second (tidal) Love number k_2, which is a dimensionless coefficient given by the ratio of the induced quardrupole moment and the applied tidal field. The dimensionless tidal Love number k_2 depends on the structure of the NS and therefore on the mass and EOS of dense matter. The quantity Λ is the induced quadrupole polarizability (tidal deformability). The dimensionless tidal deformability Λ is defined as [89]

$$\Lambda = \frac{2}{3}k_2\left(\frac{c^2R}{GM}\right)^5 = \frac{2}{3}k_2\left(\frac{1}{C}\right)^5, \tag{37}$$

where R and M are the radius and mass of the NS, G is the gravitational constant, and c is the speed of light. The quantity C is the NS compactness, which is defined as $C = \frac{GM}{c^2R}$. Clearly, Λ is extremely sensitive to the compactness parameter C and also proportional to the tidal Love number k_2, which depends on both C and y_R, the latter being a dimensionless parameter that is sensitive to the entire EOS [90,91],

$$\begin{aligned} k_2(C, y_R) = {} & \frac{8}{5}C^5(1-2C)^2[(2-y_R)+2C(y_R-1)] \\ & \times \{2C(6-3y_R+3C(5y_R-8)) \\ & + 4C^3[(13-11y_R)+C(3y_R-2) \\ & + 2C^2(1+y_R)] + 3(1-2C)^2 \\ & \times [(2-y_R)+2C(y_R-1)]\log(1-2C)\}^{-1}. \end{aligned} \tag{38}$$

Now, we proceed to describe a few details involved in to the computation of y_R (for more details, see Refs. [90–93] and references contained therein). As mentioned before, an external tidal field induces a mass quadrupole in the star. The external tidal field plus the induced stellar quadrupole combine to produce a nonspherical component to the gravitational potential that in the limit of axial symmetry is proportional to the spherical harmonic $Y_{20}(\theta, \varphi)$. In turn, the coefficient of $Y_{20}(\theta, \varphi)$, commonly referred to as $H(r)$, is a spherically symmetric function that encodes the dynamical changes to the gravitational potential and satisfies a linear, homogeneous, second-order differential equation [90],

$$\begin{aligned} & \frac{d^2H(r)}{dr^2} + \left(\frac{1+F(r)}{r}\right)\frac{dH(r)}{dr} + Q(r)H(r) = 0, \\ & \lim_{r\to 0} H(r) \simeq r^2, \end{aligned} \tag{39}$$

where $F(r)$ and $Q(r)$ are functions of the mass, pressure, and energy density profiles assumed to have been obtained by solving the TOV equations and are given by the expressions

$$F(r) = \frac{1 - 4\pi G r^2(\epsilon(r) - P(r))}{(1 - \frac{2GM(r)}{r})} \tag{40}$$

$$\begin{aligned} Q(r) = {} & \frac{4\pi}{(1-\frac{2GM(r)}{r})}\left(5\epsilon(r) + 9P(r) + \frac{\epsilon(r)+P(r)}{c_s^2(r)} - \frac{6}{4\pi r^2}\right) \\ & - 4\left[\frac{G(M(r)+4\pi r^3 P(r))}{r^2(1-\frac{2GM(r)}{r})}\right], \end{aligned} \tag{41}$$

in which $c_s^2(r) = dP(r)/d\epsilon(r)$ is the speed of sound at radius r. Once the differential equation is solved, the value of

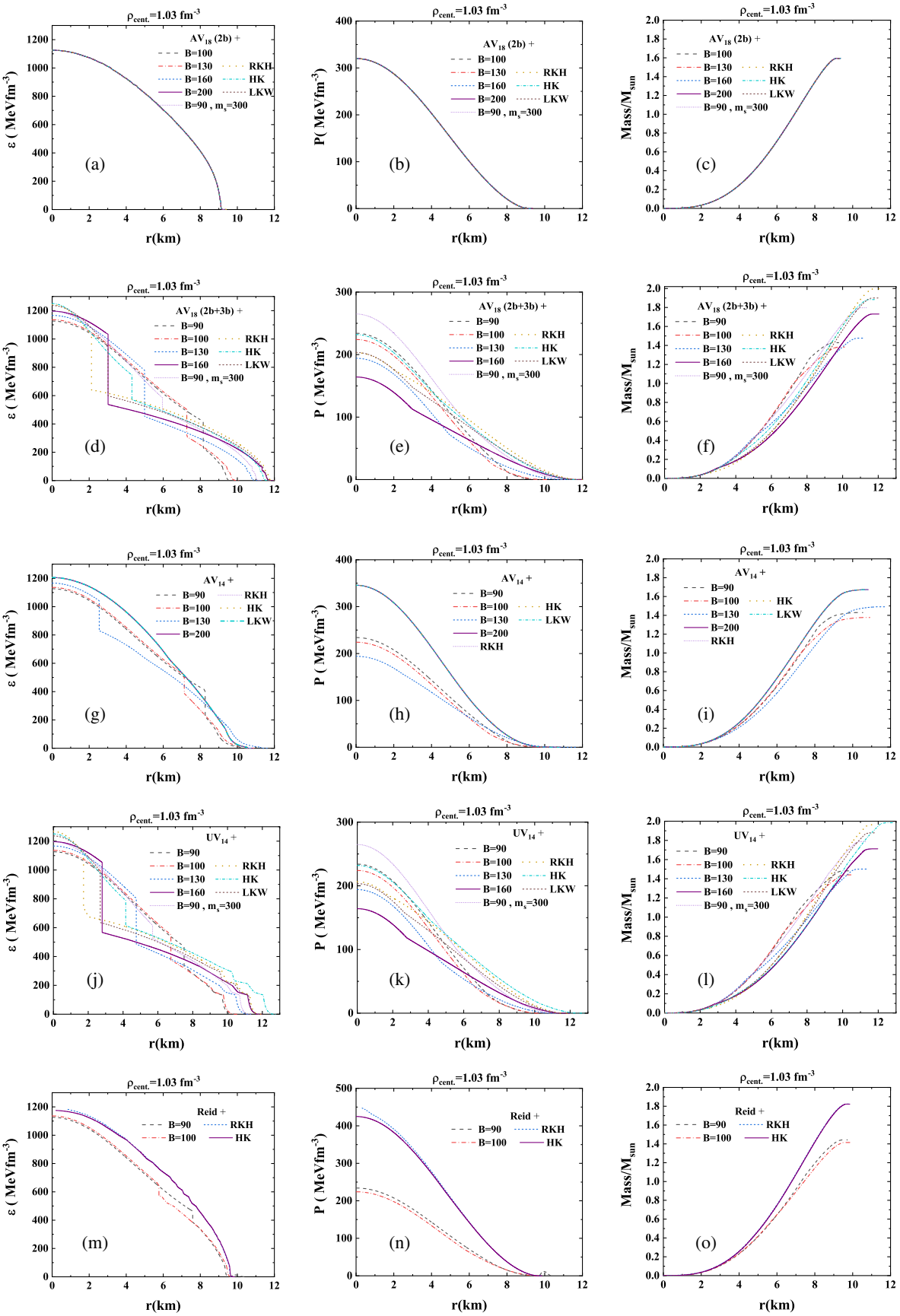

FIG. 9. (a)–(c): The energy density, pressure, and mass profiles of HSs with a central density of $\rho_{BC} = 1.03$ fm^{-3} for AV_{18} interaction without TBF and various quark models. The same quantities are shown in (d)–(f) for AV_{18}, (g)–(i) for AV_{14}, (j)–(l) for UV_{14}, and (m)–(o) for Reid interactions supplemented by TBF.

TABLE VIII. Central density ρ_c (fm^{-3}), radius R (km), compactness C, y_R, tidal Love number k_2, and dimensionless tidal deformability Λ for several purely neutron and hybrid stars with the mass of 1.4 $M_\odot$ studied in the paper.

Quark model	Hadron interactions	ρ_C (fm^{-3})	R (km)	C	y_R	k_2	Λ
Pure NS ⇛	AV_{18} (2BF)	0.86	9.497	0.218	0.388	0.0655	88.428
	AV_{18} (2BF + TBF)	0.42	12.32	0.169	0.356	0.0948	446.892
	AV_{14}	0.7	12.18	0.169	0.355	0.09518	453.142
	UV_{14}	0.44	12.28	0.169	0.361	0.09517	461.541
	Reid 68	0.7	10.34	0.202	0.377	0.0745	147.186
MIT $B = 90(\frac{\mathrm{MeV}}{\mathrm{fm}^3}), B = 150+$	AV_{18} (2BF)	0.86	9.54	0.217	0.387	0.0662	91.697
	AV_{18} (2BF + TBF)	0.97	9.86	0.209	0.384	0.0702	116.232
	AV_{14}	0.97	10.66	0.194	0.371	0.0794	192.899
	UV_{14}	0.86	10.74	0.192	0.372	0.0803	203.267
	Reid 68	0.94	9.83	0.210	0.384	0.0699	114.188
MIT $B = 100(\frac{\mathrm{MeV}}{\mathrm{fm}^3})$, $B = 150+$	AV_{18} (2BF)	0.86	9.54	0.217	0.387	0.0662	91.697
	AV_{18} (2BF + TBF)	1.08	10.02	0.206	0.399	0.0712	127.683
	AV_{14}	1.10	10.73	0.192	0.370	0.0802	201.869
	UV_{14}	0.93	10.78	0.192	0.409	0.0784	200.849
	Reid 68	1.0	9.9	0.209	0.383	0.0705	117.675
MIT $B=130,160,200, m_s=150)$ $B=90, m_s=300)$, NJL(RKH, HK, LKW)+	AV_{18} (2BF)	0.86	9.54	0.217	0.387	0.0662	91.697
	AV_{18} (2BF + TBF)	0.42	12.42	0.168	0.356	0.0951	469.980
	AV_{14}	0.7	12.28	0.168	0.354	0.0961	476.815
	UV_{14}	0.44	12.38	0.167	0.360	0.0961	485.665
	Reid 68	0.7	10.40	0.201	0.376	0.0752	153.183

y_R from the logarithmic derivative of $H(r)$ evaluated at the surface of the star is $y_R = (rH'(r)/H(r))_{r=R}$. However, since all that is needed to compute the second (tidal) Love number k_2 is the logarithmic derivative of $H(r)$, it is more efficient to solve directly for y_R, which, in turn, satisfies the following nonlinear, first-order differential equation [92,94]:

$$r\frac{dy(r)}{dr} + y^2(r) + F(r)y(r) + r^2Q(r) = 0; \quad \text{with} \quad y(0) = 2 \quad \text{and} \quad y_R = y(r = R). \tag{42}$$

Tidal effects will form a very small correction in which the accumulated phase shift can be characterized by a single quantity $\tilde{\Lambda}$, which is a weighted average of the induced quadrupole polarizability (tidal deformability) for the individual stars, Λ_1 and Λ_2. Since both NSs have the same EOS, the weighted average $\tilde{\Lambda}(\mathcal{M})$, as a function of chirp mass $\mathcal{M} = m_1^{3/5}m_2^{3/5}/(m_1 + m_2)^{1/5}$, is relatively insensitive to the mass ratio m_1/m_2 [91]. We therefore focus on the behavior of the quadrupole polarizability Λ of the individual stars [92].

Since the tidal deformability hides within a higher-order coefficient in the post-Newtonian expansion of the gravitational wave form, its extraction becomes a challenging proposition. As such, GW170817 could only establish upper limits on the tidal deformability of a 1.4 $M_\odot$ NS, i.e., $\Lambda_{1.4} \leq 800$ [93], extracted from the original discovery paper [89]. More over, the authors in Ref. [68], by employing a parametrized manner on a very large range of physically plausible EOS for compact stars and by the use of the constraints on mass, upper limit of tidal deformability and the recent suggestion on lower limit of the tidal deformability, deduced more constraints on tidal deformability and radii of neutron and hybrid stars. In that study, for a purely hadronic star with a mass of 1.4 $M_\odot$, the radius of the NS is considered to be $12.00 < R_{1.4}\ (\mathrm{km}) < 13.45$ at a 2-σ level; similarly, the smallest weighted average dimensionless tidal deformability is $\tilde{\Lambda}_{1.4} > 375$, again at a 2-$\sigma$ level. For HSs, since EOS with a phase transition allow for very compact stars on the "twin star" branch, small radii are possible [95]; therefore, the radius varies in a much broader range, $8.35 < R_{1.4}\ (\mathrm{km}) < 13.74$ at a 2-σ level, with $\tilde{\Lambda}_{1.4} > 35.5$ at a 3-σ level. As we mentioned earlier, we have computed the tidal deformabililty for individual stars with the mass of 1.4 $M \odot$, $\Lambda_{1.4}$ instead of $\tilde{\Lambda}_{1.4}$ [91,92].

We have calculated y_R, the compactness of the stars C, tidal Love number k_2, and dimensionless tidal deformability Λ for purely NSs with the mass of 1.4 $M_\odot$ with AV_{18} interaction with and without TBF and also AV_{14}, UV_{14}, and Reid interaction supplemented by TBF in order to compare them with the constraints set by the binary NS system GW170817. We have also done the calculations for several HSs in this study with the MIT and NJL models combined with these hadron interactions in LOCV formalism. The results are summarized in Table VIII. As seen in this table, the radius and dimensionless tidal deformability

of purely NSs with AV_{18} interaction without considering TBF are $R_{1.4} = 9.497$ km and $\Lambda_{1.4} = 88.428$ and for NSs with the Reid interaction are $R_{1.4} = 10.34$ km and $\Lambda_{1.4} = 147.186$, which are not in compatible with the constraints predicted for those quantities. It is worth noting that the maximum mass of purely NSs predicted with these models are 1.77 $M_\odot$ and 1.91 $M_\odot$, which are lower than the maximum mass constraint. The radius for purely NSs in AV_{18}, AV_{14}, and UV_{18} interactions supplemented by TBF are $R_{1.4} = 12.32$ km, $R_{1.4} = 12.18$ km, and $R_{1.4} = 12.28$ km, and tidal deformabilities are $\Lambda_{1.4} = 446.892$, $\Lambda_{1.4} = 453.142$, and $\Lambda_{1.4} = 461.541$, respectively, which all are in the ranges set by GW170817. The calculated maximum masses of the neutron stars with these models are 2.319 $M_\odot$, 1.76 $M_\odot$, and 2.24 $M_\odot$, respectively. Therefore, the calculated properties of purely NSs within the LOCV framework with AV_{18} and UV_{14} interactions supplemented by TBF are completely compatible with the extracted constraints from the observations. For HSs, as seen in the second and third rows of Table VIII, with $B = 90, 100$ MeV fm^{-3} combined with all the interactions, the star becomes more compact (less radii and more compactness C), and the dimensionless tidal deformability becomes much lower than the purely neutron star; however, again, they are all in the range extracted from GW170817 for the HSs, mentioned earlier. The maximum masses of all HSs within these models are about 1.5 $M_\odot$ (as seen in Table IV), which is much lower than the maximum mass constraints. As it is seen in the forth row of the Table VIII, HS's with $B = 130, 160, 200$ MeV fm^{-3} and $m_s = 150$ and $B = 90$ MeV fm^{-3} with $m_s = 300$ MeV and also NJL model in any parameter sets combined with all the interactions, are less compacted with respect to the purely NS. In these cases, the dimensionless tidal deformability increases and again are in the ranges extracted from observations for HSs. In these cases, the central density in which the star reaches 1.4 $M_\odot$ occurs in the hadron branch; therefore, it is the same as the central density in the pure hadron star. However, since the radii of HSs are a little higher with respect to the purely hadron star, HSs are less compact; therefore, their tidal deformability increases. In the cases of AV_{18}, AV_{14}, and UV_{14} interactions supplemented by TBF combined with the mentioned models, the radii are $R_{1.4}$=12.42km, $R_{1.4}$=12.28km, and $R_{1.4}$=12.38km, and the dimensionless tidal deformabilities are $\Lambda_{1.4} = 469.980$, $\Lambda_{1.4} = 476.815$, and $\Lambda_{1.4} = 485.665$, respectively, which are all in the ranges set by GW170817 even for purely hadron stars. Only the maximum masses of a HSs with AV_{18} (UV_{14}) interaction supplemented by TBF combined with the parameter set by RKH are in the range of the maximum mass constraint. For these cases, the maximum mass of the HS for AV_{18} (UV_{14}) is 2.009 $M_\odot$ (1.97 $M_\odot$). The same situation happens for a HS with AV_{18} supplemented by TBF combined with the MIT bag model with $B = 200$ MeV fm^{-3} ($B = 130, 160, 200$ MeV fm^{-3}) and $m_s = 150$ MeV ($m_s = 300$ MeV). In these cases, the maximum mass of HS is 1.962 $M_\odot$ (1.96 $M_\odot$, 2.05 $M_\odot$, 2.13 $M_\odot$). The calculated maximum mass in other models are below the observed value.

IV. CONCLUSION

We have studied the hadron-quark phase transition at high densities, which may occur in the core of massive NSs. We have adopted the LOCV formalism to describe the nuclear matter phase, while the MIT bag and NJL models have been implied for describing the quark matter phase. With $m_s = 150$ MeV, the stable HSs occur in $B = 90, 100$ MeV fm^{-3} combined with all the N-N interactions supplemented by TBF and also in $B = 130$ MeV fm^{-3} combined with AV_{14} supplemented by TBF with the maximum mass of about 1.5 $M_\odot$. The maximum mass of the HSs with$B = 200$ MeV fm^{-3} combined with AV_{18} interaction supplemented by TBF is compatible with observations. This HS is unstable because of the large energy density discontinuity in transition region which manifest itself as a cusp in mass-radius curve.

We examined the effect of N-N forces with other bare two-body interactions, AV_{14}, UV_{14}, and Reid 68 supplemented by TBF. The results are almost the same as the AV_{18} potential combined with TBF. We also checked the influence of the TBF absence in the nuclear matter. We found that in this situation the phase transition of hadron to quark matter took place in much larger densities, and stable HS with $B = 90, 100$ MeV fm^{-3} was predicted. We also examined the effect of increasing the strange mass m_s on the results gained with the MIT model. With $B = 160$ and 200 MeV fm^{-3} with $m_s = 300$ MeV, although the maximum masses of the HSs are 2.05 and 2.13 $M_\odot$, which is compatible with the observations, the HSs become unstable as soon as the onset of the quark phase because of the cusp in mass-radius curves. We found stable HSs with $m_s = 300$ MeV combined with AV_{18} and UV_{14} potentials supplemented by TBF with the maximum masses of 1.796 $M_\odot$ and 1.788 $M_\odot$, respectively. By increasing the bag constant, the HSs were rendered unstable.

Within the NJL model, a stable HS was calculated in HK parameter set combined with AV_{18} (UV_{14}) interaction with TBF with the maximum mass of 1.896 $M_\odot$ (1.882 $M_\odot$). However, the stable HS was not predicted with other hybrid EOS, again with the reason of high-energy density discontinuity in the transition region, which manifests itself as a cusp in mass-radius curves. It means that the pressure of the quark matter is unable to counteract the additional downward attraction. The maximum mass of 2.01 $M_\odot$ was calculated within the RKH parameter set combined with AV_{18} interaction supplemented by TBF, however this HS is unstable. With the NJL model, we examined the influence

of the absence of TBF, and we found that the phase transition of hadron to quark matter took place in much higher densities (about $8\rho_0$), the energy discontinuity became higher, and the value of the maximum mass became lower.

All of our results in the MIT model as well as the NJL model were in good concurrence with other works in hybrid stars with other hadron EOS.

We also computed the properties of the purely neutron and hybrid stars with the mass of 1.4 $M_\odot$ to compare them with the new constraints set by the binary neutron star system, GW170817. The radii and tidal deformability of purely NSs with the mass of 1.4 $M_\odot$, within the framework of AV_{18}, AV_{14}, and UV_{14} supplemented by TBF, are compatible with the ranges extracted from the observations. For HSs within all models existing in this study, the mentioned quantities are in compatible with the ranges for HSs. Moreover, the radii and tidal deformabilities of HSs with $B = 130, 160, 200$ MeV fm^{-3} with $m_s = 150$ MeV and $B = 90$ MeV fm^{-3} with $m_s = 300$ MeV and also NJL model in all three parameter sets combined with all interactions except Reid 68 supplemented by TBF, are in the ranges set by binary GW170817 for hadron stars.

ACKNOWLEDGMENTS

S. K. and H. R. M. warmly appreciate Micheal Buballa for his helpful comments on the NJL model and also would like to thank the Research Council, University of Tehran. S. A. T. is grateful to School of Particles and Accelerators, Institute for Research in Fundamental Sciences.

[1] N. K. Glendenning, Phase transitions and crystalline structures in neutron star cores, Phys. Rep. **342**, 393 (2001).
[2] E. Witten, Cosmic separation of phases, Phys. Rev. D **30**, 272 (1984).
[3] G. Baym, E. W. Kolb, L. D. McLerran, T. P. Walker, and R. L. Jaffe, Is Cygnus X-3 strange?, Phys. Lett. **160B**, 181 (1985).
[4] M. Hempel, G. Pagliara, and J. Schaffner-Bielich, Conditions for phase equilibrium in Supernovae, proto-neutron and neutron stars, Phys. Rev. D **80**, 125014 (2009).
[5] G. F. Burgio, M. Baldo, P. K. Sahu, and H. J. Schulze, The Hadron quark phase transition in dense matter and neutron stars, Phys. Rev. C **66**, 025802 (2002).
[6] G. F. Burgio and D. Zappala', Hybrid star structure with the field correlator method, Eur. Phys. J. A **52**, 60 (2016).
[7] P. Demorest, T. Pennucci, S. Ransom, M. Roberts, and J. Hessels, Shapiro delay measurement of a two solar mass neutron star, Nature (London) **467**, 1081 (2010).
[8] J. Antoniadis *et al.*, A massive pulsar in a compact relativistic binary, Science **340**, 1233232 (2013).
[9] R. S. Lynch *et al.*, The green bank Ttelescope 350 MHz drift-scan survey II: Data analysis and the timing of 10 new pulsars, including a relativistic binary, Astrophys. J. **763**, 81 (2013).
[10] M. H. van Kerkwijk, R. Breton, and S. R. Kulkarni, Evidence for a massive neutron star from a radial-velocity study of the companion to the black widow pulsar PSR B1957 +20, Astrophys. J. **728**, 95 (2011).
[11] E. Fonseca *et al.*, The NANOGrav nine-year data set: Mass and geometric measurements of binary millisecond pulsars, Astrophys. J. **832**, 167 (2016).
[12] C. Maieron, M. Baldo, G. F. Burgio, and H. J. Schulze, Hybrid stars with the color dielectric and the MIT bag models, Phys. Rev. D **70**, 043010 (2004).
[13] Z. H. Li and H.-J. Schulze, Neutron star structure with modern nucleonic three-body forces, Phys. Rev. C **78**, 028801 (2008).
[14] H.-J. Schulze, A. Polls, A. Ramos, and I. Vidana, Maximum mass of neutron stars, Phys. Rev. C **73**, 058801 (2006).
[15] J. D. Carroll, D. B. Leinweber, A. G. Williams, and A. W. Thomas, Phase transition from QMC hyperonic matter to deconfined quark matter, Phys. Rev. C **79**, 045810 (2009).
[16] H. Dapo, B. J. Schaefer, and J. Wambach, On the appearance of hyperons in neutron stars, Phys. Rev. C **81**, 035803 (2010).
[17] H.-J. Schulze and T. Rijken, Maximum mass of hyperon stars with the Nijmegen ES C-08 model, Phys. Rev. C **84**, 035801 (2011).
[18] H. Chen, M. Baldo, G. F. Burgio, and H.-J. Schulze, Hybrid protoneutron stars with the Dyson-Schwinger quark model, Phys. Rev. D **86**, 045006 (2012).
[19] F. Karsch, E. Laermann, and A. Peikert, The pressure in two flavor, $(2 + 1)$-flavor and three flavor QCD, Phys. Lett. B **478**, 447 (2000).
[20] F. Karsch (RBC and HotQCD Collaborations), Equation of state and more from lattice regularized QCD, J. Phys. G **35**, 104096 (2008).
[21] Y. Aoki, G. Endrodi, Z. Fodor, S. D. Katz, and K. K. Szabo, The order of the quantum chromodynamics transition predicted by the Standard Model of particle physics, Nature (London) **443**, 675 (2006).
[22] Y. Aoki, Z. Fodor, S. D. Katz, and K. K. Szabo, The QCD transition temperature: Results with physical masses in the continuum limit, Phys. Lett. B **643**, 46 (2006).
[23] A. Bhattacharyya, I. N. Mishustin, and W. Greiner, Deconfinement Phase transition in compact stars: Maxwell vs. Gibbs construction of the mixed phase, J. Phys. G **37**, 025201 (2010).
[24] R. V. Gavai and S. Gupta, QCD at finite chemical potential with six time slices, Phys. Rev. D **78**, 114503 (2008).
[25] P. de Forcrand and O. Philipsen, The QCD phase diagram for three degenerate flavors and small baryon density, Nucl. Phys. **B673**, 170 (2003).

[26] G. B. Alaverdyan, Influence of phase-transition scenarios on the abrupt changes in the characteristics of compact stars, J. Phys. Conf. Ser. **496**, 012001 (2014).
[27] M. Baldo, G. F. Burgio, P. Castorina, S. Plumari, and D. Zappala, Quark matter in neutron stars within the Nambu–Jona-Lasinio model and confinement, Phys. Rev. C **75**, 035804 (2007).
[28] T. Maruyama, S. Chiba, H. J. Schulze, and T. Tatsumi, Hadron-quark mixed phase in hyperon stars, Phys. Rev. D **76**, 123015 (2007).
[29] C. H. Lenzi, A. S. Schneider, C. Providencia, and R. M. Marinho, Compact stars with a quark core within NJL model, Phys. Rev. C **82**, 015809 (2010).
[30] D. Logoteta, C. Providencia, and I. Vidana, Formation of hybrid stars from metastable hadronic stars, Phys. Rev. C **88**, 055802 (2013).
[31] M. Baldo, G. F. Burgio, P. Castorina, S. Plumari, and D. Zappala, Astrophysical constraints on the confining models: The field correlator method, Phys. Rev. D **78**, 063009 (2008).
[32] M. G. Alford, G. F. Burgio, S. Han, G. Taranto, and D. Zappala, Constraining and applying a generic high-density equation of state, Phys. Rev. D **92**, 083002 (2015).
[33] F. Yang and H. Shen, Influence of the hadronic equation of state on the hadron-quark phase transition in neutron stars, Phys. Rev. C **77**, 025801 (2008).
[34] P. N. Bogolubov, On a model of quasiindependent quarks, Ann. Inst. Henri Poincaré Phys. Theor. **8**, 163 (1968).
[35] A. Chodos, R. L. Jaffe, K. Johnson, C. B. Thorn, and V. F. Weisskopf, A new extended model of Hadrons, Phys. Rev. D **9**, 3471 (1974).
[36] E. Farhi and R. L. Jaffe, Strange matter, Phys. Rev. D **30**, 2379 (1984).
[37] C. Alcock, E. Farhi, and A. Olinto, Strange stars, Astrophys. J. **310**, 261 (1986).
[38] N. K. Glendenning, Fast pulsars, strange stars: An opportunity in radio astronomy, Mod. Phys. Lett. A **05**, 2197 (1990).
[39] T. Hatsuda and T. Kunihiro, QCD phenomenology based on a chiral effective Lagrangian, Phys. Rep. **247**, 221 (1994).
[40] M. C. Ruivo, C. A. de Sousa, and C. Providencia, Kaons in a hot and flavor-asymmetric medium, Nucl. Phys. **A651**, 59 (1999).
[41] M. Buballa and M. Oertel, Strange quark matter with dynamically generated quark masses, Phys. Lett. B **457**, 261 (1999).
[42] M. Buballa, NJL model analysis of quark matter at large density, Phys. Rep. **407**, 205 (2005).
[43] J. C. Owen, R. F. Bishop, and J. M. Irvine, Constrained Jastrow calculations, Phys. Lett. **59B**, 1 (1975).
[44] M. Modarres and J. M. Irvine, Locv calculations with a selfconsistent treatment of isobars, J. Phys. G **5**, 511 (1979).
[45] R. V. Reid, Jr., Local phenomenological nucleon-nucleon potentials, Ann. Phys. (N.Y.) **50**, 411 (1968).
[46] A. M. Green, J. A. Niskanen, and M. E. Sainio, The effect of the delta (1236) on the imaginary component of nucleon-nucleon phase shifts, J. Phys. G **4**, 1055 (1978).
[47] H. R. Moshfegh and M. Modarres, Asymmetrical nuclear matter calculations with the new charge-dependent Reid potential, Nucl. Phys. **A759**, 79 (2005).
[48] H. R. Moshfegh and M. Modarres, Thermal properties of asymmetrical nuclear matter with the new charge-dependent Reid potential, Nucl. Phys. **A792**, 201 (2007).
[49] M. Modarres and H. R. Moshfegh, LOCV calculation for beta stable matter at finite temperature, Phys. Rev. C **62**, 044308 (2000).
[50] M. Modarres and H. R. Moshfegh, Delta(1232) isobar probability in frozen and hot neutron, nuclear and beta-stable matter, Prog. Theor. Phys. **107**, 139 (2002).
[51] S. Zaryouni and H. R. Moshfegh, A relativistic approach to the equation of state of asymmetric nuclear matter, Eur. Phys. J. A **45**, 69 (2010).
[52] S. Zaryouni, M. Hassani, and H. R. Moshfegh, Thermal properties of nuclear matter in a variational framework with relativistic corrections, Phys. Rev. C **89**, 014332 (2014).
[53] S. Goudarzi and H. R. Moshfegh, Effects of three-body forces on the maximum mass of neutron stars in the lowest-order constrained variational formalism, Phys. Rev. C **91**, 054320 (2015).
[54] S. Goudarzi, H. R. Moshfegh, and P. Haensel, The role of three-body forces in nuclear symmetry energy and symmetry free energy, Nucl. Phys. **A969**, 206 (2018).
[55] S. Goudarzi and H. R. Moshfegh, Neutron and nuclear matter properties with chiral three-nucleon forces, Nucl. Phys. **A985**, 1 (2019).
[56] M. Shahrbaf, H. R. Moshfegh, and M. Modarres, Equation of state and correlation functions of hypernuclear matter within the lowest order constrained variational method, Phys. Rev. C **100**, 044314 (2019).
[57] M. Shahrbaf and H. R. Moshfegh, Appearance of hyperons in neutron stars within LOCV method, Ann. Phys. (Amsterdam) **402**, 66 (2019).
[58] T. Maruyama, T. Tatsumi, T. Endo, and S. Chiba, Pasta structures in compact stars, arXiv:nucl-th/0605075
[59] M. G. Alford, K. Rajagopal, S. Reddy, and F. Wilczek, The minimal CFL nuclear interface, Phys. Rev. D **64**, 074017 (2001).
[60] F. Neumann, M. Buballa, and M. Oertel, Mixed phases of color superconducting quark matter, Nucl. Phys. **A714**, 481 (2003).
[61] S. Benic, D. Blaschke, D. E. Alvarez-Castillo, T. Fischer, and S. Typel, A new quark-hadron hybrid equation of state for astrophysics–I. High-mass twin compact stars, Astron. Astrophys. **577**, A40 (2015).
[62] D. L. Whittenbury, H. H. Matevosyan, and A. W. Thomas, Hybrid stars using the quark-meson coupling and proper-time Nambu-Jona-Lasinio models, Phys. Rev. C **93**, 035807 (2016).
[63] C. M. Li, J. L. Zhang, T. Zhao, Y. P. Zhao, and H. S. Zong, Studies of the hybrid star structure within $2+1$ flavors NJL model, Phys. Rev. D **95**, 056018 (2017).
[64] S. Ejiri and N. Yamada, End Point of a First-Order Phase Transition in Many-Flavor Lattice QCD at Finite Temperature and Density, Phys. Rev. Lett. **110**, 172001 (2013).
[65] P. de Forcrand, J. Langelage, O. Philipsen, and W. Unger, Lattice QCD Phase Diagram in and Away from the Strong Coupling Limit, Phys. Rev. Lett. **113**, 152002 (2014).

[66] G. Endrodi, Critical point in the QCD phase diagram for extremely strong background magnetic fields, J. High Energy Phys. 07 (2015) 173.
[67] V. V. Braguta, V. A. Goy, E.-M. Ilgenfritz, A. Y. Kotov, A. V. Molochkov, M. Muller-Preussker, and B. Petersson, Two-color QCD with non-zero Chiral chemical potential, J. High Energy Phys. 06 (2015) 094.
[68] E. R. Most, L. R. Weih, L. Rezzolla, and J. Schaffner-Bielich, New Constraints on Radii and Tidal Deformabilities of Neutron Stars from GW170817, Phys. Rev. Lett. **120**, 261103 (2018).
[69] B. P. Abbott *et al.* (LIGO Scientific and Virgo Collaborations), Properties of the Binary Neutron Star Merger GW170817, Phys. Rev. X **9**, 011001 (2019).
[70] B. P. Abbott *et al.* (LIGO Scientific and Virgo Collaborations), GW170817: Measurements of Neutron Star Radii and Equation of State, Phys. Rev. Lett. **121**, 161101 (2018).
[71] J. W. Negele and D. Vautherin, Neutron star matter at subnuclear densities, Nucl. Phys. **A207**, 298 (1973).
[72] C. Drischler, A. Carbone, K. Hebeler, and A. Schwenk, Neutron matter from chiral two- and three-nucleon calculations up to N^3LO, Phys. Rev. C **94**, 054307 (2016).
[73] E. Annala, T. Gorda, A. Kurkela, and A. Vuorinen, Gravitational-Wave Constraints on the Neutron-Star-Matter Equation of State, Phys. Rev. Lett. **120**, 172703 (2018).
[74] C. Drischler, K. Hebeler, and A. Schwenk, Chiral Interactions Up to Next-to-Next-to-Next-to-Leading Order and Nuclear Saturation, Phys. Rev. Lett. **122**, 042501 (2019).
[75] F. Weber, R. Negreiros, P. Rosenfield, and M. Stejner, Pulsars as astrophysical laboratories for nuclear and particle physics, Prog. Part. Nucl. Phys. **59**, 94 (2007).
[76] G. H. Bordbar and M. Modarres, Lowest order constrained variational calculation for asymmetrical nuclear matter with the new Argonne potential, Phys. Rev. C **57**, 714 (1998).
[77] J. C. Owen, R. F. Bishop, and J. M. Irvine, A variational approach to nuclear matter with realistic potentials, Nucl. Phys. **A277**, 45 (1977).
[78] P. Rehberg, S. P. Klevansky, and J. Hufner, Hadronization in the SU(3) Nambu-Jona-Lasinio model, Phys. Rev. C **53**, 410 (1996).
[79] M. F. M. Lutz, S. Klimt, and W. Weise, Meson properties at finite temperature and baryon density, Nucl. Phys. **A542**, 521 (1992).
[80] K. Hagiwara *et al.* (Particle Data Group), Review of particle physics, Phys. Rev. D **66**, 010001 (2002).
[81] G. F. Burgio, M. Baldo, P. K. Sahu, A. B. Santra, and H. J. Schulze, Maximum mass of neutron stars with a quark core, Phys. Lett. B **526**, 19 (2002).
[82] G. F. Burgio, The Hadron-quark phase transition in neutron stars, Nucl. Phys. **A749**, 337 (2005).
[83] M. Alford and S. Reddy, Compact stars with color superconducting quark matter, Phys. Rev. D **67**, 074024 (2003).
[84] M. Baldo, M. Buballa, F. Burgio, F. Neumann, M. Oertel, and H. J. Schulze, Neutron stars and the transition to color superconducting quark matter, Phys. Lett. B **562**, 153 (2003).
[85] K. Schertler, S. Leupold, and J. Schaffner-Bielich, Neutron stars and quark phases in the NJL model, Phys. Rev. C **60**, 025801 (1999).
[86] A. Steiner, M. Prakash, and J. M. Lattimer, Quark-hadron phase transitions in young and old neutron stars, Phys. Lett. B **486**, 239 (2000).
[87] L. Bildsten and C. Cutler, Tidal interactions of inspiraling compact binaries, Astrophys. J. **400**, 175 (1992).
[88] E. E. Flanagan and T. Hinderer, Constraining neutron star tidal Love numbers with gravitational wave detectors, Phys. Rev. D **77**, 021502(R) (2008).
[89] B. P. Abbott *et al.* (LIGO Scientific and Virgo Collaborations), GW170817: Observation of Gravitational Waves from a Binary Neutron Star Inspiral, Phys. Rev. Lett. **119**, 161101 (2017).
[90] T. Hinderer, Tidal Love numbers of neutron stars, Astrophys. J. **677**, 1216 (2008).
[91] T. Hinderer, B. D. Lackey, R. N. Lang, and J. S. Read, Tidal deformability of neutron stars with realistic equations of state and their gravitational wave signatures in binary inspiral, Phys. Rev. D **81**, 123016 (2010).
[92] S. Postnikov, M. Prakash, and J. M. Lattimer, Tidal Love numbers of neutron and self-bound quark stars, Phys. Rev. D **82**, 024016 (2010).
[93] J. Piekarewicz and F. J. Fattoyev, Impact of the neutron star crust on the tidal polarizability, Phys. Rev. C **99**, 045802 (2019).
[94] F. J. Fattoyev, J. Carvajal, W. G. Newton, and B. A. Li, Constraining the high-density behavior of the nuclear symmetry energy with the tidal polarizability of neutron stars, Phys. Rev. C **87**, 015806 (2013).
[95] G. Montana, L. Tolos, M. Hanauske, and L. Rezzolla, Constraining twin stars with GW170817, Phys. Rev. D **99**, 103009 (2019).